日本磁気学会
ISSN 2432-0250
Journal of the Magnetics Society of Japan
Electronic Journal URL: https://www.jstage.jst.go.jp/browse/msjmag

Vol.41 No.2　2017

Journal

JOURNAL OF THE MAGNETICS SOCIETY OF JAPAN

Vol.41 No.2 2017

日本磁気学会

ISSN 2432-0250

HP: http://www.magnetics.jp/ e-mail: msj@bj.wakwak.com

Electronic Journal: http://www.jstage.jst.go.jp/browse/msjmag

世界初！
高温超電導型VSM

新製品

世界初*、高温超電導マグネットをVSMに採用することで
測定速度 当社従来機1/20を実現。
0.5mm cube磁石のBr, HcJ高精度測定が可能と
なりました。
*2014年7月 東英工業調べ

測定結果例

高温超電導VSMによるNdFeB(sint.) 0.5mm cube BHカーブ

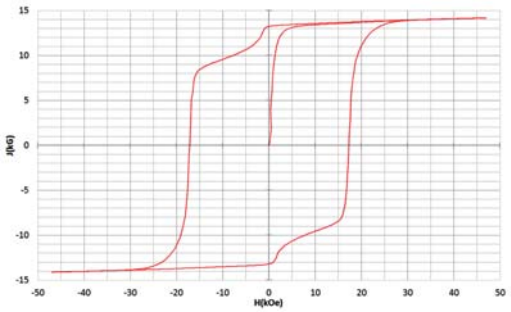

磁化測定レンジ：0.2emu
Br = 13.2kG　　HcJ = 17.2kOe

高温超電導VSMによるNdFeB(sint.) 1mm cube BHカーブ

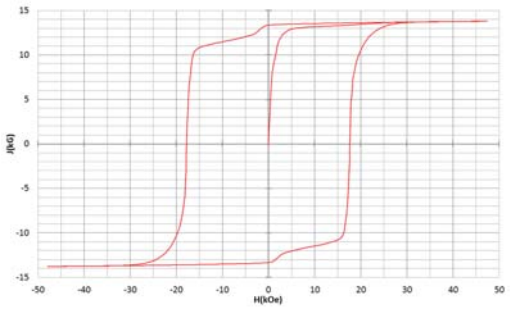

磁化測定レンジ：2emu
Br = 13.3kG　　HcJ = 17.7kOe

高温超電導VSMによるNdFeB(sint.) 4mm cube BHカーブ

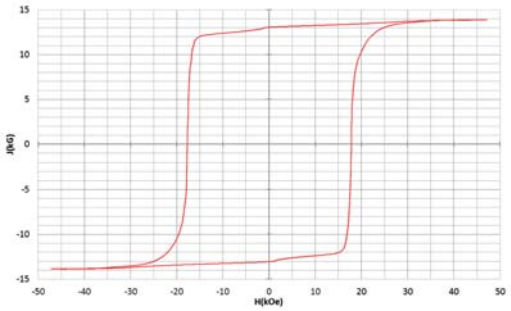

磁化測定レンジ：100emu
Br = 13.1kG　　HcJ = 17.8kOe

高速測定を実現

高温超電導マグネット採用により、高速測定を実現しました。Hmax= 5Tesla, Full Loop 測定が2分で可能です。
（当社従来機：Full Loop測定　40分）

小試料のBr,HcJ高精度測定

0.5mm cube 磁石のBr,HcJ高精度測定ができ、表面改質領域を切り出しBr,HcJの強度分布等、微小変化量の比較測定が可能です。
また、試料の加工劣化の比較測定が可能です。

試料温度可変測定

−50℃～+200℃温度可変UNIT（オプション）

磁界発生部の小型化

マグネットシステム部寸法：0.8m×0.3m×0.3m

TOEI 東英工業株式会社
http://www.toeikogyo.co.jp
〒194-0035 東京都町田市忠生1-8-13
TEL：042-791-1211　FAX：042-792-0490
E-mail : sales@toeikogyo.co.jp

COMSOL MULTIPHYSICS®

有限要素法解析ソフトウェア COMSOL Multiphysics®

マルチフィジックスの進化論

無制限・強連成で実現象に即したシミュレーション事例のご紹介

永久磁石を利用した磁気軸受の解析例

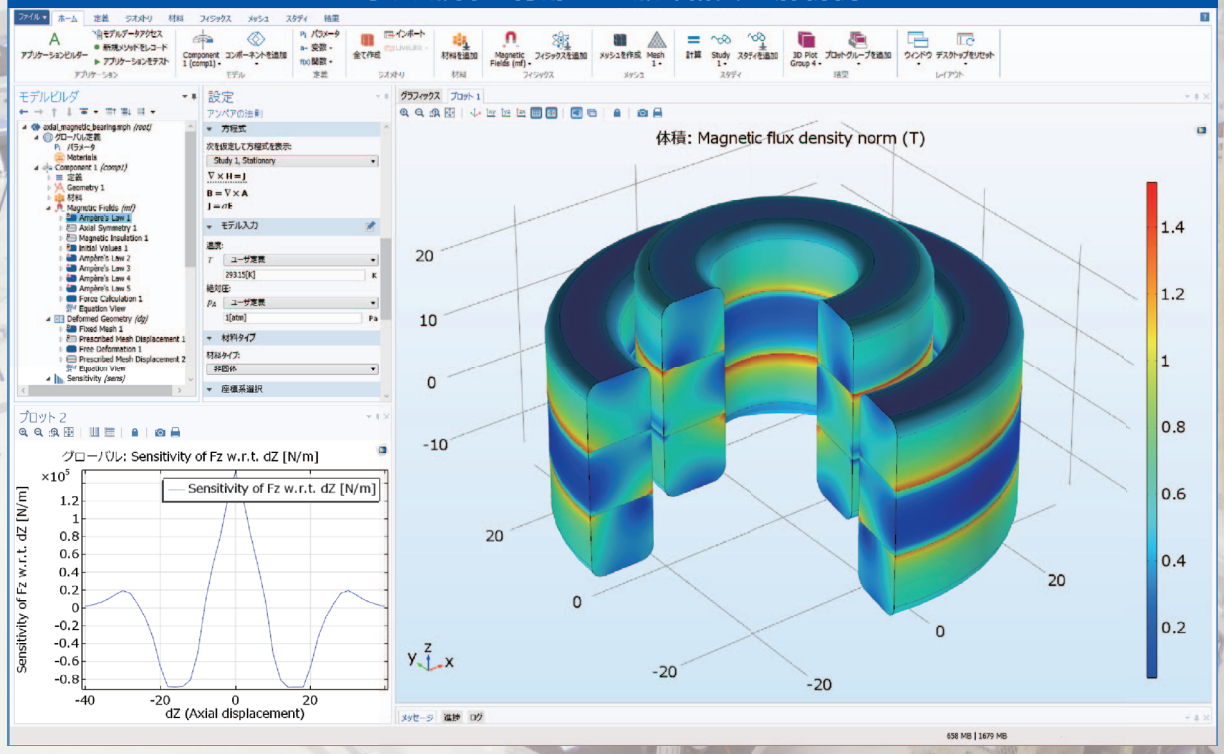

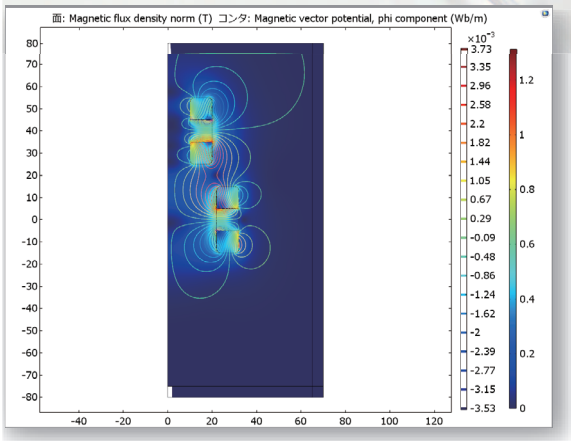

永久磁石を使用した磁気軸受

永久磁石を使用した軸受はターボ機械、ポンプ、モータ、発電機やフライホイール式エネルギー貯蔵システムなど、様々な分野で使用されています。非接触かつ潤滑不要で保守整備を大幅に省略できる点は、従来の機械式ベアリングと比べて重要なメリットです。
この例では、軸方向の永久磁石軸受の磁気力と剛性などの設計パラメータを計算する方法を示しています。

※AC/DCモジュールはCOMSOL Multiphysicsと併用するアドオン製品です。

AC/DC モジュールの適用例

- AC/DC 電流分布、電場分布
- バイオヒーティング
- コイルとソレノイド
- SPICE 回路とフィールドシミュレーション
- 接触抵抗
- 電磁両立性 (EMC) および電磁妨害 (EMI)
- 電磁力およびトルク
- 電磁力シールド
- 電気機械の変形
- ホール効果を利用したセンサ
- インシュレータ、コンデンサ、誘電体
- モータ、ジェネレータ、および他の電気機械
- 非線形材料
- 寄生容量とインダクタンス
- 永久磁石と電磁石
- 多孔質材料
- 抵抗および誘導加熱
- センサ
- 超伝導体
- 変圧器とインダクタ

COMSOL Multiphysics® なら、今まで不可能だった 3 種以上のマルチフィジックス解析を強連成で実現できます。30 日間全機能無料トライアル、無料の導入セミナー、1000種を超える世界の様々な事例をご提供いたします。詳しくは、下記の弊社営業部までお問い合せください。

COMSOL

http://www.comsol.jp

KESCO KEISOKU ENGINEERING SYSTEM
計測エンジニアリングシステム株式会社
http://www.kesco.co.jp/comsol/
Tel : 03-5282-7040 ・ Fax : 03-5282-0808

新製品

磁区観察ユニット

既存のプローバ装置で磁区観察を！
小型でシンプル！磁区観察をより手軽に！

※概要・特徴

- プローバ装置などに取り付けることが可能な小型・低価格の磁区観察ユニット
- 面内 / 垂直どちらの磁化方向にも対応
- 社内設計光学系による面内磁区の高コントラスト観察（空間分解能 3μm 以下 ）
- 光学系ヘッドの大きさは、 150×150×300mm 重量も 2kg と軽量・コンパクト
- 白色 LED 光源を用いた高安定性・長寿命
- オプションとして顕微鏡スタンド・ステージ・高機能観察 / 解析ソフトウェアなどを用意

※観察例

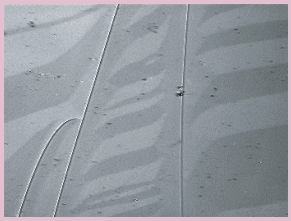

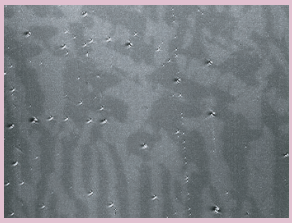

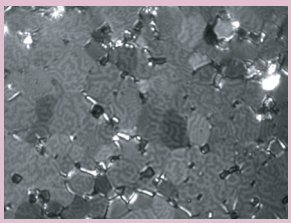

※オプション例

- θ-X-Y-Z 軸ステージ
- 顕微鏡スタンド

※この組み合わせでも重量は約 9kg ですので、 設置場所を選びません

この製品以外に、 30 年の研究現場への対応経験に基づいた高精度・高性能の磁気 Kerr 効果装置、Faraday 装置、 磁区観察顕微鏡など、 各種磁気光学製品の取り揃えがございます。
お気軽にお問合せください。

レーザとレーザ応用システム製品の総合メーカー
NEOARK ネオアーク株式会社
営 業 部 / 〒156-0041 東京都世田谷区大原2-17-6-108 TEL(03)6379-5539 FAX(03)6379-5688
大阪支店 / 〒541-0056 大阪市中央区久太郎町2-3-8-201 TEL(06)6271-5123 FAX(06)6271-5110
本社 第1工場・第2工場 / 八王子市
URL http://www.neoark.co.jp E-mail:info@neoark.co.jp

INDEX

にかほで「みらい」を体験しよう！

みらい

2035年のみらいを体験

アインシュタイン=ド・ハース効果
実験装置を体験

歴史

TDKとエレクトロニクスの歴史を体験

チームラボによるデジタル空間で磁性を体験

TDK Museum

TDK歴史みらい館

http://www.tdk.co.jp/museum/ TDK歴史みらい館

〒018-0402　秋田県にかほ市平沢字画書面15　TEL：0184-35-6580　FAX：0184-35-6853
JR仁賀保駅より 徒歩約10分（タクシーで約3分）

■ 開館時間：10時～18時　　■ 休館日：月曜日（祝日を除く）・当館の定める日
■ 入館料：無料（団体の方は、事前申し込みが必要です）

2016年
10月7日（金）
RENEWAL OPEN!

TDK

Journal of the Magnetics Society of Japan
Vol. 41, No. 2

Electronic Journal URL: https://www.jstage.jst.go.jp/browse/msjmag

CONTENTS

J. Magn. Soc. Jpn., **41**, 20-24 (2017)

<Paper>

Synthesis and magnetic properties of Fe substituted hibonite

H. Nagumo*, K. Watanabe**, K. Kakizaki*, and K. Kamishima*

* Graduate School of Science and Engineering, Saitama University, *255 Shimo-Okubo, Saitama 338–0825, Japan*

** Biomolecular Characterization Unit, Center for Sustainable Resource Science, RIKEN, *2-1 Wako, Saitama 351–0198, Japan*

We have investigated the synthesis conditions and magnetic properties of Fe substituted hibonite with initial compositions of $CaAl_{12-x}Fe_xO_{19}$ ($0 \leq x \leq 12$) and $CaAl_{10-x}Fe_xO_{19-\delta}$ ($0 \leq x \leq 10$). The Fe doped hibonite can be synthesized at a sintering temperature of 1300˚C. The X–ray diffraction patterns of Fe substituted hibonite samples are in good agreement with the pattern of hibonite. The lattice parameter increased due to the difference between the radius of Al^{3+} and that of Fe^{3+}. The magnetization and Curie temperature of the best sample ($CaAl_2Fe_8O_{19-\delta}$) are 31 emu/g and 290˚C, respectively.

Keywords: M–type, hexaferrite

1. Introduction

M-type ferrites (Ba, Sr, Pb)$Fe_{12}O_{19}$ have high magnetization and coercivity, which leads to application as a permanent magnet. Consequently, M-type ferrites have long been the subject of intensive research.[1)]

Ca-based M–type ferrite is an attractive subject because of the rich resource of its Fe and Ca elements. Fe and Ca are widespread elements in minerals, as implied by the 4th and 5th largest Clarke numbers of Fe and Ca.[2)] However, there is no $CaFe_{12}O_{19}$ phase in the CaO-Fe_2O_3 diagram.[3), 4)] This Ca-based M-type ferrite can be stabilized only by the addition of a rare-earth element of La.[5)–7)]

The crystal structure of M-type ferrite is similar to that of hibonite ($CaAl_{12}O_{19}$) except that the structure models are divided on the interpretation of the bipyramidal Al^{3+} ions.[8)] Figure 1 shows the crystal structure of $CaAl_{12}O_{19}$ along [010] view direction. The unit cell contains two chemical formulas of $CaAl_{12}O_{19}$ like M-type ferrite. To the best of our knowledge, the systematic substitution effect of Fe^{3+} for Al^{3+} of $CaAl_{12}O_{19}$ has not been reported yet in spite of the similarity in the crystal structures.[9)]

In this study, we have investigated the synthesis conditions and magnetic properties of the Fe substituted hibonite.

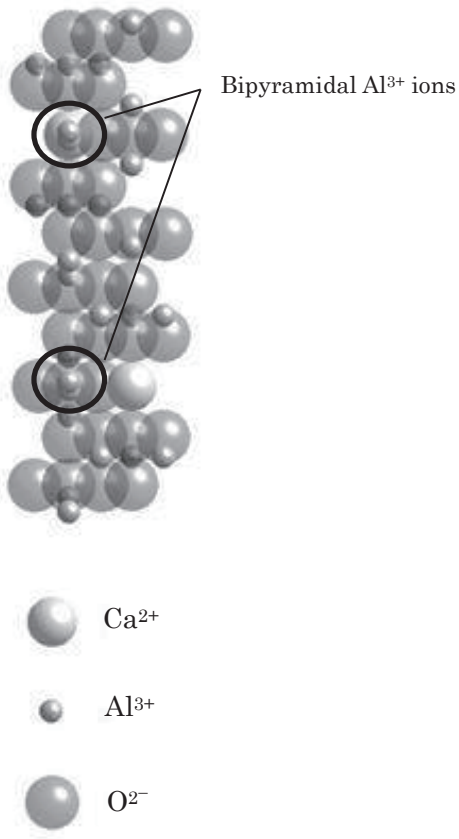

Fig. 1 Crystal structure of hibonite along [010] view direction.

2. Experimental procedure

Samples were prepared by a conventional ceramic method. We used $CaCO_3$, Al_2O_3, and α–Fe_2O_3 as starting materials. Before we mixed them, we heated Al_2O_3 powder at 500˚C for an hour in order to remove water molecules on the material. They were mixed in the desired proportions of $CaAl_{12-x}Fe_xO_{19}$ ($0 \leq x \leq 12$) and $CaAl_{10-x}Fe_xO_{19-\delta}$ ($0 \leq x \leq 10$) in a ball-milling pot for 24 h. The mixed powder was pressed into a disk shape. The disk was pre-sintered in air at 900˚C for 5 h. The sintered sample was pounded in a mortar and then ground into fine powder using a planetary ball mill for 10 minutes at 1100 rpm (Fritsch, P–7 Premium line). The powder was pressed into a disk shape. The disks were heated at 1100—1400˚C for 5 h. X-ray diffraction (XRD) analysis with Cu-Kα radiation was performed to characterize the crystalline samples. The magnetic properties were measured by using a vibrating sample magnetometer (Tamakawa TM-VSM2130HGC). The chemical composition was examined by using a commercial electron probe micro analyzer (EPMA) (JEOL, JXA – 8200).

3. Results and discussion

Figure 2 shows the X–ray diffraction patterns of the sintered samples at 1300˚C whose starting powder was mixed at the iron-substituted-hibonite chemical composition of Ca: Al: Fe=1:(12–x):x. The hibonite chemical composition sample (x=0) exhibits the mixed phases of Al_2O_3, $CaAl_4O_7$, and $CaAl_2O_4$. The hibonite phase was formed by the substitution of Fe for Al at x≥1. The diffraction peaks of the hibonite phase shifted to the low angle side with increasing the Fe content.

The (Al+Fe)/Ca ratio of twelve to one may be too large for the reaction to form the hibonite phase because the starting material of α–Fe_2O_3 remained at x≥7 (iron rich compositions). In the same way, that of Al_2O_3 did not react at x≤2 (aluminum rich compositions).

Figure 3 shows the lattice constants of the hibonite phase in the $CaAl_{12-x}Fe_xO_{19}$ ($0 \le x \le 12$) initial composition samples sintered at 1300˚C. The lattice constants a and c were obtained using Cohen's least square method.[10] a and c gradually increased with the amount of Fe^{3+} ions

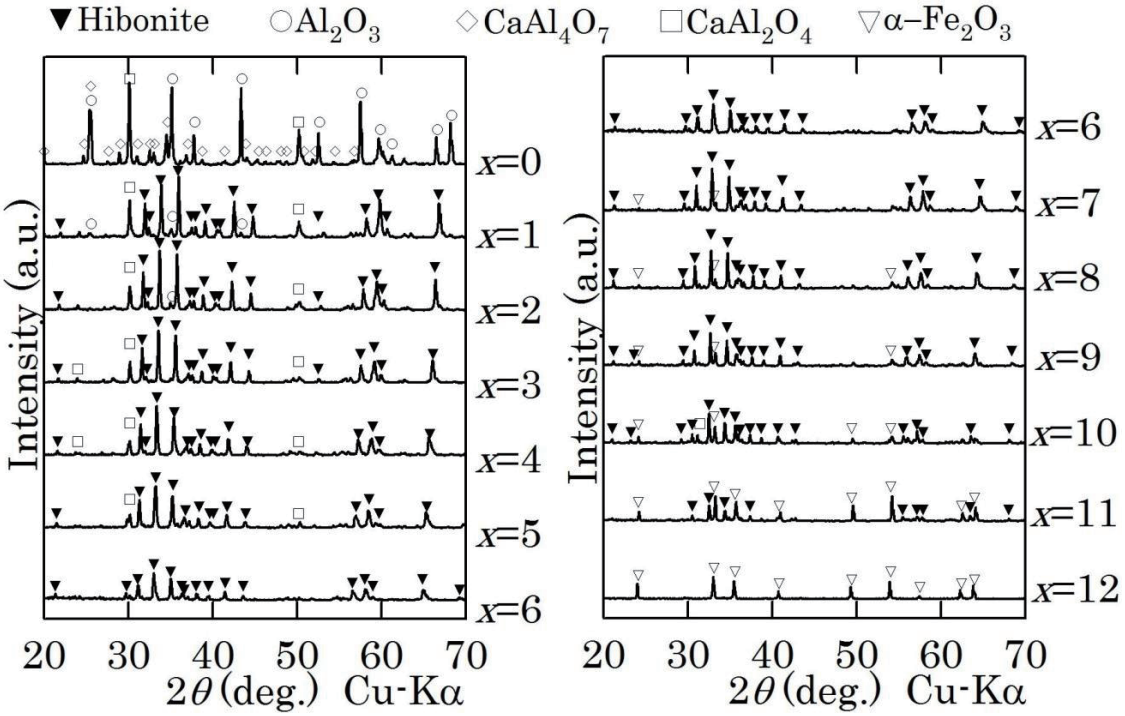

Fig. 2 X-ray diffraction patterns of the $CaAl_{12-x}Fe_xO_{19}$ ($0 \le x \le 12$) initial composition samples sintered at 1300˚C.

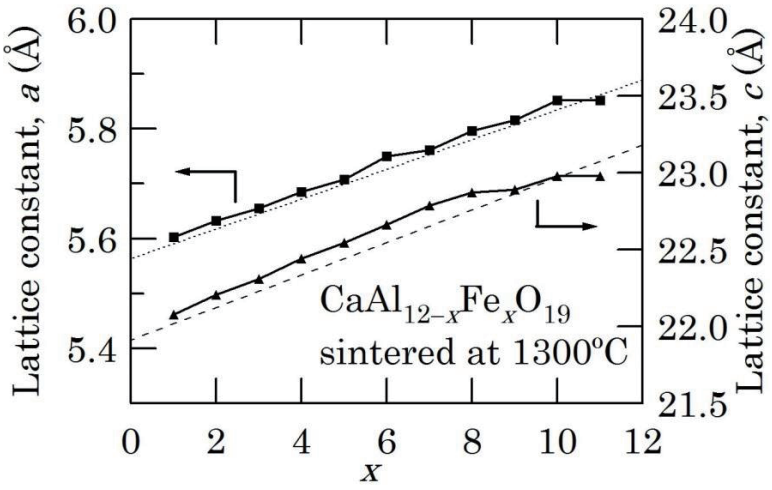

Fig. 3 Lattice constants of the $CaAl_{12-x}Fe_xO_{19}$ ($1 \le x \le 11$) initial composition samples sintered at 1300˚C.

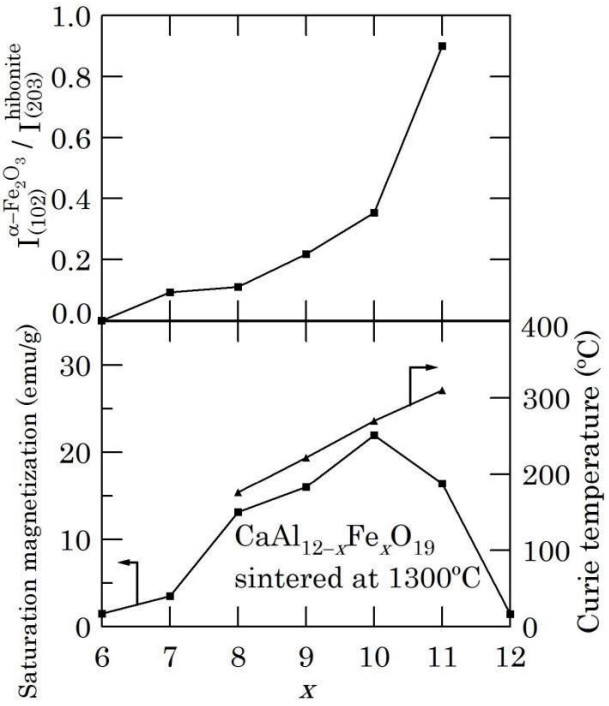

Fig. 4 Saturation magnetization and Curie temperature of the $CaAl_{12-x}Fe_xO_{19}$ ($6 \leq x \leq 12$) initial composition samples sintered at 1300˚C. The intensity ratio of the α–Fe_2O_3 (102) plane to the hibonite (203) plane is also shown.

because the ionic radius of an Fe^{3+} ion $r[Fe^{3+}]$ is larger than that of an Al^{3+} ion $r[Al^{3+}]$; $r[Fe^{3+}, HS]=0.49$ Å > $r[Al^{3+}]=0.39$ Å at a tetrahedral site and $r[Fe^{3+}, HS]=0.645$ Å > $r[Al^{3+}]=0.535$ Å at an octahedral site, where "HS" denotes the high spin configuration of electrons. [11] The dotted straight lines are connected between the lattice constants of the hibonite ($x=0$) and the typical M-type ferrite ($SrFe_{12}O_{19}$) in which the ionic radius of Sr is similar to that of Ca. Our results are close to these dotted lines, which implies that a linear relation exists between the lattice constant and the concentrations of the constituent elements (Vegard's law).[12]

Figure 4 shows the saturation magnetization (M_S) at room temperature, the Curie temperature (T_C), and the relative intensity $I^{\alpha-Fe_2O_3}_{(102)}/I^{hibonite}_{(203)}$ of the Fe rich composition samples ($CaAl_{12-x}Fe_xO_{19}$; $x \geq 6$). The samples at $x<7$ had small magnetizations at room temperature in spite of the single crystallographic phase of hibonite. This fact reflects the small intrinsic magnetic moment and low T_C due to the small amount of the iron cations. With increasing the iron content up to $x=10$, M_S increased although the relative intensity of α–Fe_2O_3 gradually increased. This increase of M_S is due to the replacement of non-magnetic Al^{3+} to magnetic Fe^{3+} ions of magnetic hibonite phase in these samples. On the other hand, M_S decreased with increasing the iron content above $x=10$. This is consistent with the fact that the diffraction peaks of hibonite became weak and finally disappeared at $x=12$.

The Curie temperature was increased by iron substitution. Because nonmagnetic Al^{3+} ions were

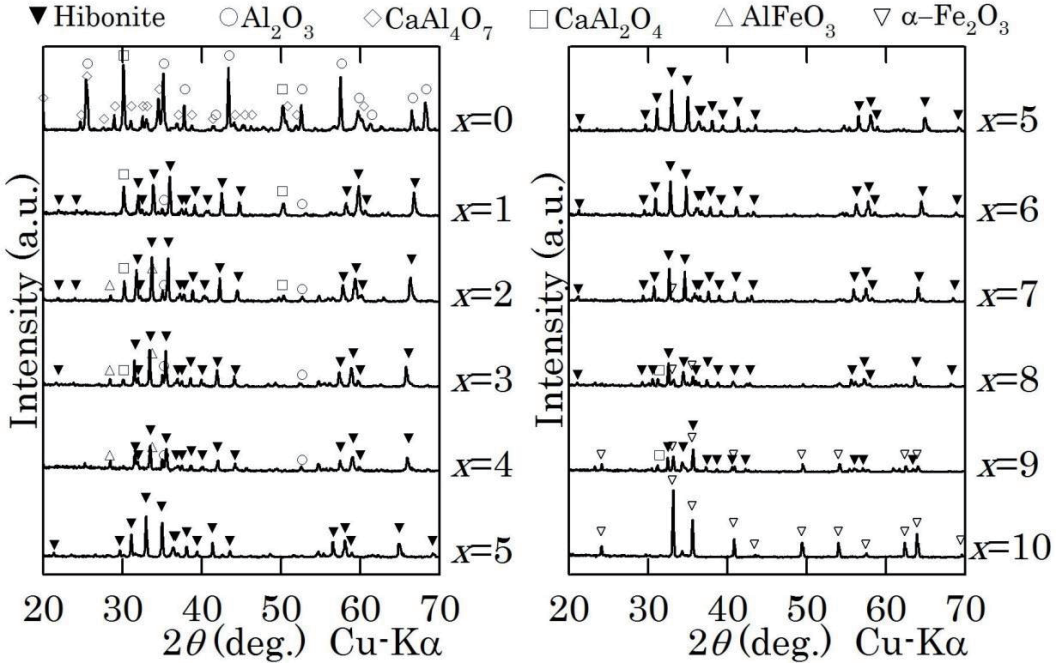

Fig. 5 X-ray diffraction patterns of the $CaAl_{10-x}Fe_xO_{19-\delta}$ ($0 \leq x \leq 10$) initial composition samples sintered at 1300˚C.

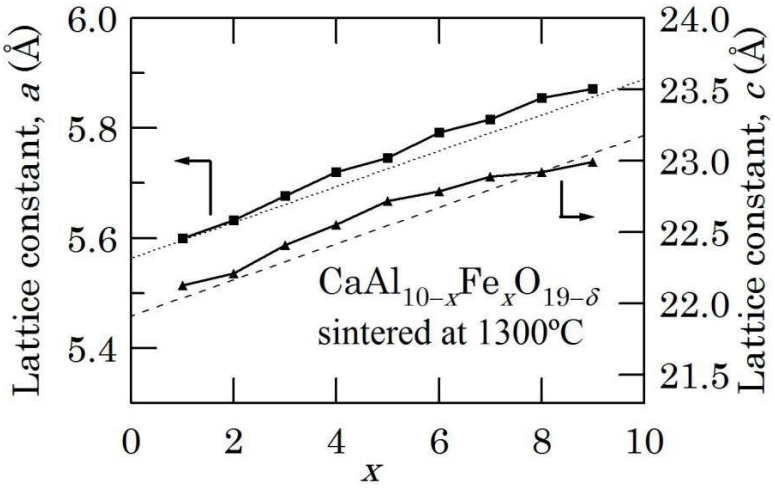

Fig. 6 Lattice constant of the $CaAl_{10-x}Fe_xO_{19-\delta}$ ($1 \leq x \leq 9$) initial composition samples sintered at 1300˚C.

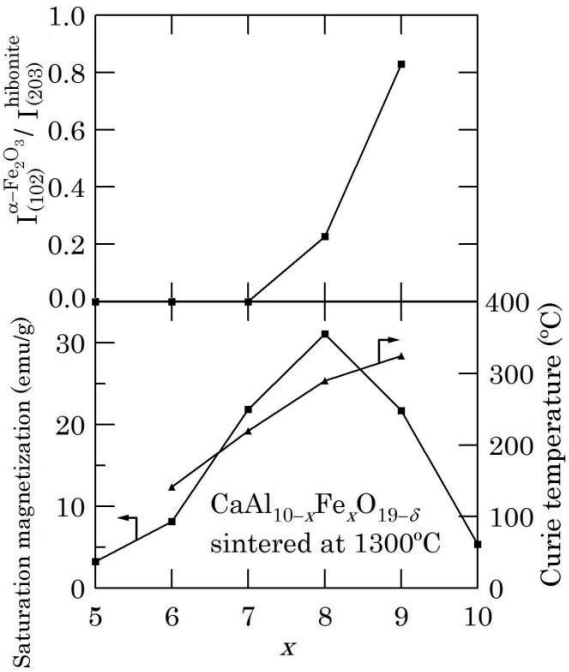

Fig. 7 Saturation magnetization and Curie temperature of the $CaAl_{10-x}Fe_xO_{19-\delta}$ ($5 \leq x \leq 10$) initial composition samples sintered at 1300˚C. The intensity ratio of the α–Fe_2O_3 (102) plane to the hibonite (203) plane is also shown.

Table 1 Chemical composition of the x=8 sample ($CaAl_2Fe_8O_{19-\delta}$) sintered at 1300˚C.

	Ca→1	Initial
Ca	1	1
Al	1.75	2
Fe	7.11	8

replaced by magnetic Fe^{3+} ions, the average superexchange interaction between magnetic Fe^{3+} ions in the sample can operate. The increase of the amount of the iron cations and their interactions may lead to the rise of T_C. T_C was increased up to x=11 even though M_S was decreased from x=10 to x=11. This means that the magnetic hibonite phase was formed with excessive α–Fe_2O_3 at x=11. The excess of α–Fe_2O_3 at x=11 is also implied by the abrupt increase of $I_{(102)}^{\alpha\text{-}Fe_2O_3}/I_{(203)}^{hibonite}$ from x=10 to x=11 in Fig. 4. This result also suggests that the (Al+Fe)/Ca ratio of twelve to one is too large for the formation of the hibonite phase. This is consistent with the XRD result shown in Fig. 2.

These experimental results of $CaAl_{12-x}Fe_xO_{19}$ led us to the next experiments to decrease the (Al+Fe)/Ca ratio in iron-substituted hibonite. We changed the starting composition from $CaAl_{12-x}Fe_xO_{19}$ to $CaAl_{10-x}Fe_xO_{19-\delta}$ in order to prevent the excess of α–Fe_2O_3 and to improve the magnetic properties.

Figure 5 shows the X-ray diffraction patterns of the sintered samples at 1300˚C whose starting powder was mixed at the chemical composition of Ca:Al:Fe=1:(10–x):x. After we changed the starting composition from $CaAl_{12-x}Fe_xO_{19}$ to $CaAl_{10-x}Fe_xO_{19-\delta}$, peaks of hematite became weaker at the iron rich compositions.

Figure 6 shows the lattice constants of the $CaAl_{10-x}Fe_xO_{19-\delta}$ ($0 \leq x \leq 10$) initial composition samples sintered at 1300˚C. The dotted straight lines are connected between the lattice constants of the hibonite (x=0) and $SrFe_{12}O_{19}$. The substitution–dependent variation of lattice constants ($\Delta a/\Delta x$ and $\Delta c/\Delta x$) of $CaAl_{10-x}Fe_xO_{19-\delta}$ at the Fe rich compositions is larger than that of $CaAl_{12-x}Fe_xO_{19}$ ($x \geq 10$). In addition, the X-ray diffraction peaks of the remaining α–Fe_2O_3 in $CaAl_{10-x}Fe_xO_{19-\delta}$ are weaker than those in $CaAl_{12-x}Fe_xO_{19}$ at the Fe rich compositions. These facts indicate that the substitution of Fe^{3+} for Al^{3+} in $CaAl_{10-x}Fe_xO_{19-\delta}$ is

more successful than in $CaAl_{12-x}Fe_xO_{19}$.

Figure 7 shows the saturation magnetization (M_S) at room temperature and the Curie temperature (T_C) and the relative intensity $I^{\alpha-Fe_2O_3}_{(102)}/I^{hibonite}_{(203)}$ of the Fe rich composition samples. The iron-substitution dependence is similar to that of $CaAl_{12-x}Fe_xO_{19}$ in Fig. 4. However, the value of M_S was higher than that of $CaAl_{12-x}Fe_xO_{19}$ composition samples. The maximum T_C was 325°C for $CaAl_{10-x}Fe_xO_{19-\delta}$ at x=9. It should be noted that this maximum Curie temperature is higher than the maximum T_C of $CaAl_{12-x}Fe_xO_{19}$ at x=11. The relative intensity $I^{\alpha-Fe_2O_3}_{(102)}/I^{hibonite}_{(203)}$ is also lower than that in Fig. 4. These facts suggest that the starting material composition of Ca: Al: Fe=1:(10–x):x is more suitable for the synthesis of iron-substituted magnetic hibonite.

Table 1 shows the estimated chemical composition of the x=8 sample ($CaAl_2Fe_8O_{19-\delta}$) sintered at 1300°C. By the use of EPMA, we measured the compositions of 50 particles of this sample. The table shows the average composition. The elements of Ca, Al, and Fe were in the ratio 1: 1.75: 7.11. The ratio of Ca is slightly higher than the initial ratio of 1: 2: 8. This may be caused by the elution of the Ca-rich oxide (e.g., $CaFe_2O_4$ with melting point of 1216°C) on the sample grains.[3)]

4. Conclusion

Fe^{3+} substituted hibonite–phase samples have been successfully synthesized by a conventional ceramic method with the modified initial chemical compositions of $CaAl_{10-x}Fe_xO_{19-\delta}$. XRD patterns of $CaAl_{10-x}Fe_xO_{19-\delta}$ sintered at 1300°C demonstrated the hibonite phase at $1 \leq x \leq 9$. The lattice parameter increased with increasing Fe^{3+} content. The maximum saturation magnetization was 31 emu/g at x=8 ($CaAl_2Fe_8O_{19-\delta}$). The Curie temperature rose up to 325°C with the replacement of Al^{3+} ions by Fe^{3+} ions.

References

1) J. Smit and H. P. J. Wijn: Ferrites, 177—211 (Philips Technical Library, 1959).
2) F. W. Clark and H. S. Washington: The Composition of the Earth's Crust, 34 (Government Printing Office, 1924).
3) B. Phillips and A. Muan: *J. Am. Ceram.* Soc., **41**, 445—454 (1958).
4) B. S. Boyanov: *J. Min. Met.* , **41 B**, 67—77 (2005).
5) N. Ichinose and K. Kurihara: *J. Phys. Soc. Jpn.*, **18**, 1700—1701 (1963).
6) H. Yamamoto, T. Kawaguchi, and M. Nagakura: *IEEE Trans. Magn.*, **15**, 1141—1146 (1979).
7) Y. Kobayashi, S, Hosokawa, E. Oda, and S. Toyota: *J. Jpn. Soc. Powder Powder Metall.*, **v. 55-7**, 541—546 (2008).
8) A. Utsunomiya, K. Tanaka, H. Morikawa, F. Marumo, and H. Kojima: *J. Solid State Chem.*, **75**, 197—200 (1988).
9) J. B. MacChesney, R.C. Sherwood, E. T. Keve, P. B. O'Connor, and L. D. Blitzer: Proc. Int. Conf. Ferrites, Kyoto, 1970, 158 (1971).
10) B. D. Cullity: Elements of X-ray Diffraction, 342 (Addison-Wesley, 1967).
11) R. D. Shannon, *Acta Cryst.* **A 32**, 751-767 (1976).
12) L. Vegard, *Z. Physik*, **5**, 17 (1921).

Received Jul. 30, 2016; Revised Oct. 3, 2016; Accepted Dec. 9, 2016

J. Magn. Soc. Jpn., **41**, 25-28 (2017)

<Paper>

Permeability Measurements of Thin Film Using a Flexible Microstrip Line-Type Probe Up To 40 GHz

S. Yabukami, K. Kusunoki*, H. Uetake, H. Yamada*, T. Ozawa, R. Utsumi**, T. Moriizumi***, and Y. Shimada****

Tohoku Gakuin University, *1-13-1 Chuo, Tagajo 985-8537, Japan*

*Sendai National College of Technology, *48 Nodayama, Medeshima-Shiote, Natori 981-1239, Japan*

**Toei Scientific Industrial Company Ltd., *1-101-60 Medeshimadai, Natori 981-1251, Japan*

***Candox Systems Inc., *15-21 Oshiage-Cho, Gyoda 361-0045, Japan*

****Graduate School of Engineering, Tohoku University, *6-6-05 Aramaki Aza Aoba, Aoba-ku, Sendai 980-8579, Japan*

A highly sensitive probe based on the skin effect was developed to measure thin film permeability. A new microstrip-line-type probe on a flexible substrate was fabricated and placed in contact with a magnetic thin film. The probe enhanced the signal-to-noise ratio and broadband measurement. The permeability of amorphous CoNbZr film (25 mm × 25 mm, 5 nm thick) and that of CoFeB film (45 mm × 25 mm, 0.5 μm thick) were optimized. The measured values were in rough agreement with theoretical values based on the Landau–Lifshitz–Gilbert equation and eddy current generation up to 40 GHz.

Key words: flexible microstrip-line-type probe, skin effect, permeability, very thin film

1. Introduction

High frequency permeability of very thin magnetic films is important because sensing devices and spintronic devices are fabricated from such film (film thickness of less than 10 nm). However, almost all permeameters[1)–3)] require a special sample, usually no more than several millimeters in width and more than 100 nm in thickness. Exceedingly few permeameters can measure thin film over 30 GHz continuously.

As previously reported, we have developed a microstrip-line-type probe[4)]. The probe is not always applicable for evaluation of very thin film, such as that less than 10 nm in thickness, because of the low signal-to-noise ratio. Subsequently, we also developed a straight microstrip-line-type probe on a flexible polyimide substrate[5)]. However, the probe resonates at a frequency of over 7 GHz because of impedance mismatch and is not applicable for large samples.

In the present study, we developed a new probe composed of a straight microstrip line on a flexible substrate, the microstrip line sloping to meet the lead line at either end. The flexibility of the probe enables contact between it and a magnetic thin film, which enhances the signal-to-noise ratio. The probe, including the microstrip line and lead lines, has a characteristic impedance of around 50 ohm. As a result, the permeability of very thin film was evaluated up to 40 GHz.

2. Experimental setup

2.1 A new probe and system setup

Fig. 1(a) shows a schematic diagram of the probe. Figs. 1(b) and (c) show a photograph of the probe. The new probe is composed of a straight microstrip conductor (15 mm in length, 0.36 mm in width) on a flexible substrate (RT/duroid@ 5870, 130 μm in

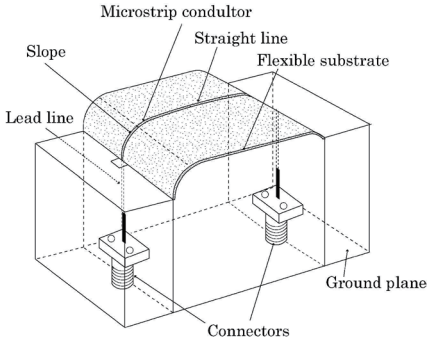

(a) oblique drawing

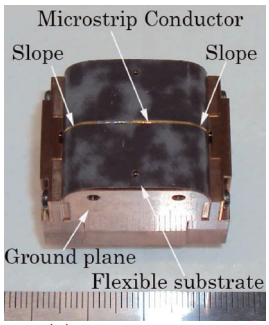

(b) top view

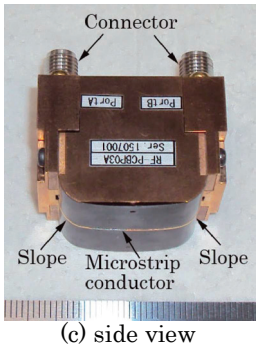

(c) side view

Fig. 1 Schematic view of probe.

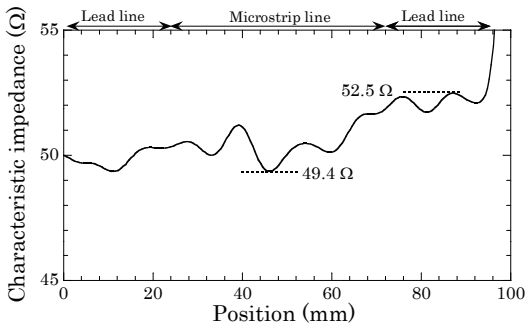

Fig. 2 Characteristic impedance of the probe obtained from time-domain reflectometry (TDR) measurements.

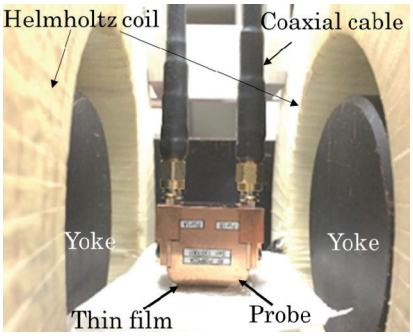

Fig. 3 Photograph of the probe and film.

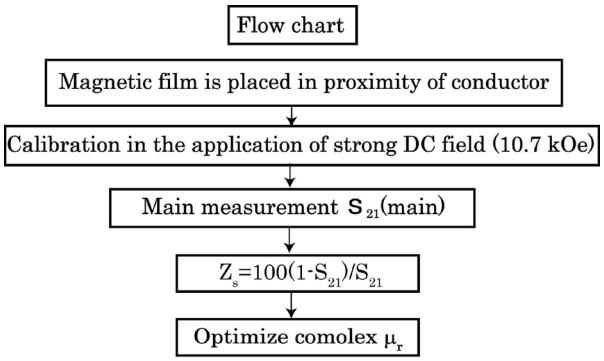

Fig. 4 Flow chart of the permeability measurements.

thickness, ε_r=2.3), a ground plane, lead lines, and two connectors. The microstrip line has slopes to maintain a characteristic impedance of around 50 Ω and to allow close contact of a large sample with the probe. A magnetic thin film coated with photo-resist (about 8 μm in thickness) is in contact with the microstrip conductor. Coaxial cables are connected to a network analyzer. The probe can be easily bent because of the flexibility of the substrate, enabling a good fit between the probe and the thin film, resulting in improved signal-to-noise ratio.

Fig. 2 shows the characteristic impedance of the probe measured by time domain reflectometry (Agilent Technologies N5227A). The characteristic impedance was 49.4 Ω-52.5 Ω along the microstrip line.

The system setup was the same as the previous works[4),5)]. Fig. 3 shows a photograph of the probe, a magnetic film, a Helmholtz coil, and a micrometer. The spacing between the probe and the film is adjusted by a micrometer. An Fe yoke (80 mm in diameter) is arranged around the bias coil to increase the dc magnetic field.

2.2 Optimization of permeability

Fig. 4 shows a flow chart of permeability optimization. Firstly, S_{21} is calibrated by application of a strong dc field (around 850.65 kA/m (10.7 kOe)) in the direction of the easy axis to saturate the magnetic film. Secondly, S_{21} is measured without a strong dc field, and then the complex impedance is calculated by equation (1).

$$Z_s = 100\ (1 - S_{21})/S_{21} \tag{1}$$

The S_{21} and Z_s include the multiple reflections in equation (1). Complex permeability is optimized using the Newton–Raphson method[6)] to take the skin effect of the magnetic film into account by using equations (2) - (4),

$$Z_s = \frac{k_s \rho l}{2w}\coth\left(\frac{k_s t}{2}\right) - \left\{\frac{k'_s \rho l}{2w}\coth\left(\frac{k'_s t}{2}\right)\right\}\frac{1}{S_{21}} \tag{2}$$

$$k_s = \frac{(1+j)}{\sqrt{\frac{\rho}{\pi f \mu_r \mu_0}}} \tag{3}$$

$$k'_s = \frac{(1+j)}{\sqrt{\frac{\rho}{\pi f \mu_r^{ref} \mu_0}}} \tag{4}$$

where ρ is the resistivity of the film, t is the film thickness, l is the microstrip line length, w is the width of the microstrip conductor, and μ_r^{ref} is relative permeability when a strong dc field of 10.7 kOe was applied. The high frequency current induces a magnetic field in the width direction of the conductor pattern, and the magnetic field and the eddy current are localized in the skin of the magnetic film[4),5)].

3. Experimental results

Fig. 5 shows the MH curves of $Co_{85}Nb_{12}Zr_3$ film and CoFeB film. Fig. 5(a) shows the MH curve of CoNbZr film (25 mm × 25 mm and 5 nm in thickness). The CoNbZr film was deposited by RF sputtering. The solid line shows the MH curve of the easy axis, and the dotted line shows that of the hard axis. The resistivity of the film was about 1.52×10^{-6} Ωm (152 μΩcm), which was slightly higher than that of bulky CoNbZr (120 μΩcm). An anisotropy field of around 70 Oe was observed. The anisotropy field was comparatively larger than that of previous studies[7),8)], which is probably because the CoNbZr film was partly crystallized. However the perpendicular anisotropy that has often been observed for partially crystallized CoNbZr films is not seen for the sample probably because of intensified shape anisotropy of 5 nm thickness. Fig. 5(b) shows the MH curve of the CoFeB film (45 mm × 25 mm and 0.5 μm in thickness). The film was deposited by Carousel Sputtering[9)]. Saturation magnetization around 2.2 T and an anisotropy field (H_k) of around 260 Oe was observed from the MH curve.

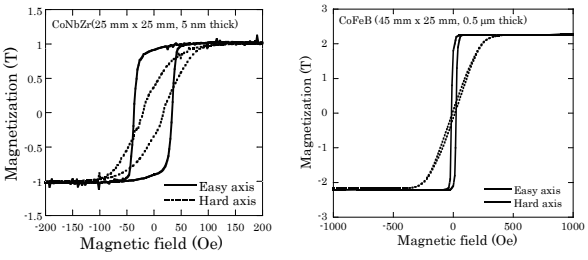

(a) CoNbZr film (b) CoFeB film

Fig. 5 MH curve of the film sample.

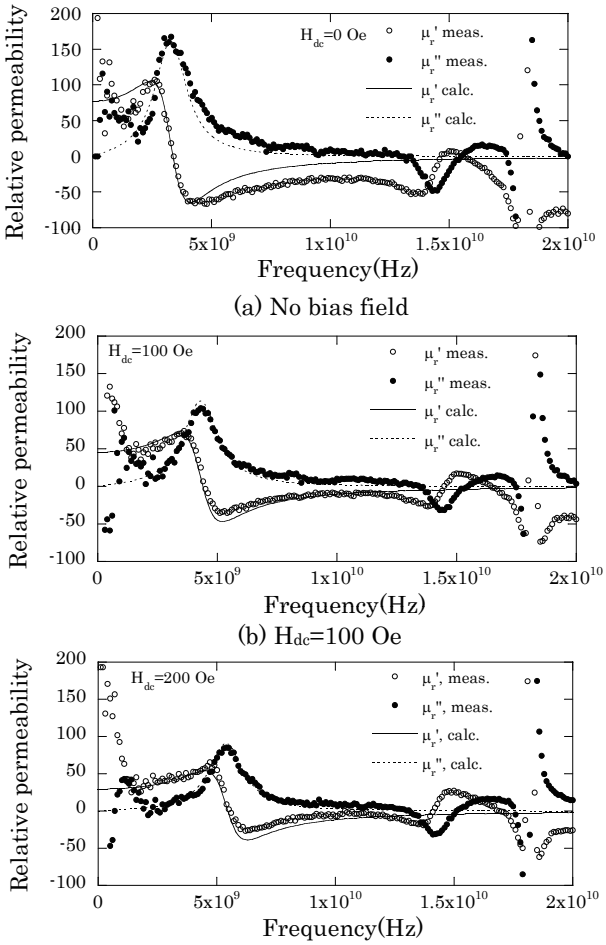

(a) No bias field

(b) H_{dc}=100 Oe

(c) H_{dc}=200 Oe

Fig. 6 Relative permeability of CoNbZr film (25 mm x 25 mm, 5 nm thick).

Fig. 6 shows the hard-axis permeability of amorphous CoNbZr film (25 mm × 25 mm, 5 nm in thickness) when it was in contact with the flexible probe. Fig. 6 (a) shows the permeability without the bias field, and (b) and (c) show the permeability when bias fields of 100 and 200 Oe, respectively, were applied along the easy axis. The symbols show measured permeability, and the dotted lines and the solid lines show the theoretical permeability based on the Landau–Lifshitz–Gilbert equation and eddy current generation[10],respectively. A g factor of 2.13[11] was used to calculate theoretical permeability. An α (damping factor) of 0.04 was used to fit theoretical permeability to measured spectra. The absolute permeability was calibrated by the application of dc magnetic fields in the direction of the easy axis. The measured permeability roughly corresponded to the theoretical permeability up to 14 GHz. The ferromagnetic resonances were observed, and the resonance frequency was found to shift as the bias field increased. The signal to noise ratio in lower frequency decreased and the ferromagnetic resonance frequency was higher than that in the previous report[5], which was because the present system consist of magnetic core, therefore small leakage field of the yoke increased the resonance frequency even if the DC current was zero.

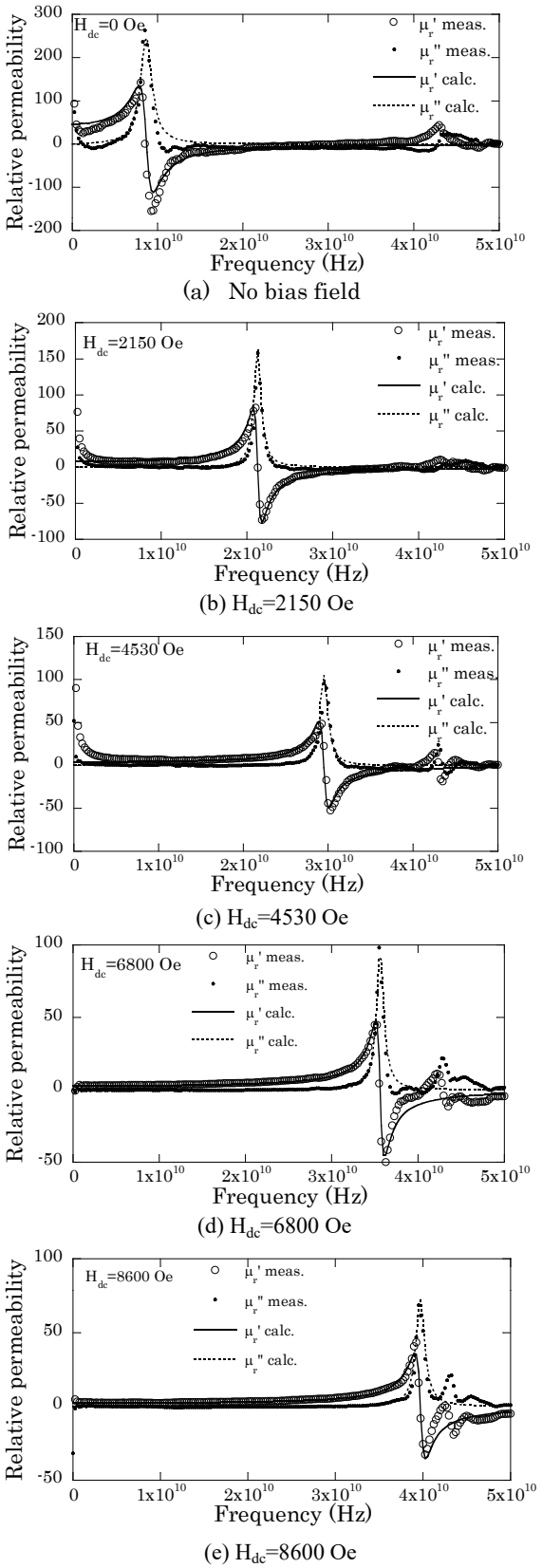

(a) No bias field

(b) H_{dc}=2150 Oe

(c) H_{dc}=4530 Oe

(d) H_{dc}=6800 Oe

(e) H_{dc}=8600 Oe

Fig. 7 Relative permeability of CoFeB film (45 mm × 25 mm, 0.5 μm thick).

Fig. 7 shows the hard–axis permeability of CoFeB film (45 mm x 25 mm, 0.5 μm in thickness). Fig. 7 (a) shows the permeability without a bias field, and

Figs. 7 (b)–(e) show the permeability when bias fields of 2150, 4530, 6800, and 8600 Oe were applied along the easy axis. Symbols show measured permeability, and the dotted lines and solid lines show the theoretical permeability based on the Landau–Lifshitz–Gilbert equation and eddy current generation[10],respectively. An α (damping factor) of 0.02 and a g factor of 2.13 were used to calculate theoretical permeability. The absolute permeability was calibrated by the application of dc magnetic fields in the direction of the easy axis. The measured permeability was found to roughly correspond to theoretical permeability up to 40 GHz. Ferromagnetic resonance shifted from 8 to 40 GHz as the dc field increased. A sharp change was observed around 42–43 GHz. This limit originated from the ferromagnetic resonance of the magnetic film with a strong bias field of about 10.7 kOe.

4. Conclusions

1. A highly sensitive probe was developed to measure very thin film permeability using a straight microstrip line and a flexible substrate.
2. A CoNbZr film (25 mm x 25 mm, 5 nm in thickness) was evaluated and the measured permeability was in rough agreement with the theoretical permeability up to 14 GHz.
3. A CoFeB film (45 mm x 25 mm, 0.5 μm in thickness) with a high anisotropy field was evaluated, and measured permeability was in rough agreement with the theoretical permeability up to 40 GHz.

Acknowledgments We would like to thank Prof. Munakata at Sojo University for providing the CoFeB film, Mr. Fujita of Japan Science and Technology Bureau for his advice, Dr. Nakai of Industrial Technology Institute, Miyagi Prefectural Government for his help in measurement of MH-curves, and the Machine Shop of Tohoku Gakuin University for help in fabricating the probe. This work was supported in part by the Program for Revitalization Promotion of JST.

References

1) P. A. Calcagno, D. A. Thompson: *Rev. Sci. Instrum.,* **46**, 904 (1975).
2) M. Yamaguchi, S. Yabukami and K.I. Arai: *IEEE Trans. Magn.*, **32**, 4941 (1996).
3) H. B. Weir: *Proc IEEE.*, **62**, 33 (1975).
4) T. Kimura, S. Yabukami, T. Ozawa, Y. Miyazawa, H. Kenju, Y. Shimada: *J. Magn. Soc. Jpn.* **38**, pp. 87-91 (2014).
5) K. Kusunoki, S. Yabukami, T. Ozawa, H. Uetake, H. Yamada, Y. Miyazawa, Y. Shimada: *J. Magn. Soc. Jpn.* **39**, pp. 111-115 (2015).
6) W.H. Press, S.A. Teukolsky, W.T. Vetterling and B.P. Flannery: Numerical Recipes in C (Japanese Edition)., pp.251–281, (Gijutsu Hyoron sha , Tokyo,1993).
7) H. Katada, T. Shimatsu, I. Watanabe, H. Muraoka, Y. Nakamura and Y. Sugita: *J. Magn. Soc. Jpn.*, **24**, 539 (2000).
8) M.L. Schneider, A.B. Kos, and T.J. Silva: *Applied Physics Letters*, 85, 254 (2004).
9) M. Namikawa, M. Munakata, M. Yagi, M. Motoyama, Y. Shimada, S. Yabukami, M. Yamaguchi, and K.I. Arai : *J. Magn. Soc. Jpn.,* **27**, 371 (2003).
10) Y. Shimada, J. Numazawa, Y. Yoneda and A. Hosono: *J. Magn. Soc. Jpn.*, **15**, 327(1991).
11) A. Yoshihara, K. Takanashi, M. Shimada , O. Kitakami and Y. Shimada: *Jpn. J. Appl. Phys*. **33**, 3927 (1994).

Received Feb. 10, 2016; Revised Aug. 26, 2016; Accepted Jan. 10, 2017

J. Magn. Soc. Jpn., **41**, 29-33 (2017)

<Paper>

Development of MO imaging plate for MO color imaging

Y. Nagakubo, Y. Baba, Q. Liu, G. Lou, and T. Ishibashi

Department of Materials Science and Technology, Nagaoka University of Technology, *1603-1 Kamitomioka, Nagaoka, Niigata 940-2188, Japan*

We propose a magneto-optical (MO) color imaging technique that enables magnetic field distributions to be quantitatively observed in real-time. Values of magnetic fields are displayed as colors. MO imaging plates have been developed using highly bismuth-substituted neodymium iron garnet films, for use in MO color imaging. The films were prepared by the metal-organic decomposition method. The MO imaging plates were characterized using the MO figure of merit for MO imaging plates, which is defined in this study. The magnetic fields were expressed by colors, using light-emitting diodes (LEDs) as light sources. The colors varied from blue to yellow, from green to yellow, and from blue to red, for sources corresponding to a white LED, combined green and yellow LEDs, and combined blue and yellow LEDs, respectively. The MO color imaging of spherical magnets is demonstrated.

Key words: magneto-optical imaging, bismuth substituted neodymium iron garnet, magneto-optical effect, metal organic decomposition, magneto-optical imaging plate, magneto-optical figure of merit

1. Introduction

The MO imaging technique utilizes the magneto-optical (MO) effect of bismuth-substituted iron garnet. The technique was developed separately by Japanese and Russian groups in 1990, to visualize stray magnetic fields from superconducting materials[1), 2)]. MO imaging allows magnetic field distributions to be observed in real-time, by placing MO imaging plates at locations to be measured[1)-9)]. MO imaging can achieve a high spatial resolution of ~0.3 μm[8), 10)], and a high speed response with frequencies up to ~1 GHz[11)]. Computational calculations for each pixel in a measured MO image are conventionally required to obtain a quantitative image of the magnetic field[4)-6)]. To realize quantitative MO imaging, we propose a MO color imaging technique that enables quantitative magnetic field distributions to be observed in real-time and values of magnetic fields are displayed as colors. We expect the resolution of the displayed magnetic field to be improved by using color instead of monochrome. Specifically, the resolution of the magnetic field in color could potentially be the cube of that in monochrome. For example, in the case of an 8-bit camera, magnetic field values could be expressed with $2^{8\times3}$ = 16777216 colors, compared with 2^8 = 256 in monochrome.

MO imaging plates are expected to have properties suitable for MO color imaging. Large MO imaging plates are required to observe magnetic field distributions with the naked eye. Bi-substituted rare-earth iron garnets ($R_{3-x}Bi_xFe_5O_{12}$: Bi:RIGs) have traditionally been used as materials for MO imaging plates. These are usually prepared by the liquid phase epitaxy method. However, it is difficult to achieve a high Bi substitution, and the size of films is limited by that of the single crystal substrate such as $Gd_3Ga_5O_{12}$ (GGG), which is typically smaller than 4 inches in diameter[12)-14)]. To overcome these problems, we prepared highly Bi-substituted neodymium iron garnet ($Nd_{3-x}Bi_xFe_{5-y}Ga_yO_{12}$) films, by metal-organic decomposition (MOD) on glass and GGG substrates[15)]. This allows larger MO imaging plates to be prepared.

In this paper, we discuss the MO figure of merit for MO imaging plates prepared using $Nd_{0.5}Bi_{2.5}Fe_5O_{12}$ (Bi2.5:NIG) or $NdBi_2Fe_5O_{12}$ (Bi2:NIG), and we report the use of the MO imaging plates in quantitative MO color imaging.

2. Experimental

Bi2.5:NIG and Bi2:NIG thin films were prepared by the MOD method on glass and GGG substrates[16)-18)]. Bi2.5:NIG and Bi2:NIG were selected as the MO films for the MO imaging plate. This was because their MO figures of merit were sufficiently high, and their spectral profiles were suitable for MO color imaging. MOD solutions were produced by Kojundo Chemical Laboratory Co., Ltd. The glass substrates used in this study were Eagle XG, Corning. $Nd_2BiFe_4GaO_{12}$ (Bi1:NIGG) thin films with a thickness of 90 nm were prepared as a buffer layer on the glass substrates.

To prepare Bi2.5:NIG, Bi2:NIG and Bi1:NIG thin films, each MOD solution was spin-coated at 3000 rpm on the substrate for 60 s. The resulting film was dried at 100 ºC for 10 min, and then pre-annealed at 450 ºC for 10 min. This process of spin-coating to pre-annealing was repeated five times. The resulting film was then crystallized in a furnace at 600–700 ºC for 3 h in air. The process was repeated several times, to increase the film thickness. Ag alloy (APC, Furuya Metal Co., Ltd.) films of approximately 100 nm in thickness were deposited on the garnet layers as reflection layers, using a coater (SC-704, Sanyu Electron Co., Ltd.).

The MO and optical properties of the MO imaging plates were measured, to evaluate the MO figure of merit. Faraday and Kerr rotation spectra were measured using a MO spectrometer (Neoark Co., Ltd.). The spectrometer consisted of a halogen lamp, polarizer,

monochromator, electromagnet, and polarization angle detector. The spectrometer setup was based on the balanced detection method. Transmission spectra were measured using a spectrometer (V-570, JASCO Corp.).

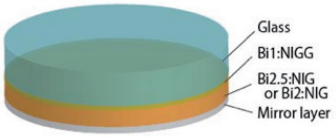

Fig. 1 Structure of the MO imaging plate prepared on a glass substrate.

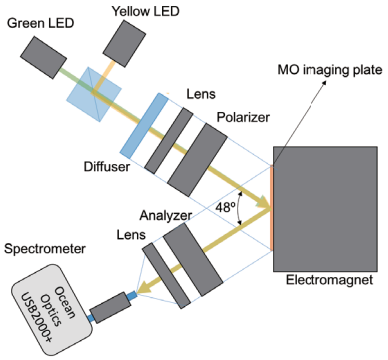

Fig. 2 Schematic illustration of the experimental setup.

The experimental setup shown in Fig. 2 was used for MO color imaging. The light source was a white LED, or combined green and yellow LEDs, or combined blue and yellow LEDs. The applied magnetic field range of the electromagnet (AZ1-0, Toei Scientific Industrial Co., Ltd.) was set from −3 kOe to +3 kOe. MO images were collected using a CMOS camera, and spectra were measured using a spectrometer (USB2000+, OceanOptics). The angle of the polarizer and analyzer were set at 0 and 84°, respectively. This combination of angles was found to result in the largest color change, upon application of the magnetic field. The relationship between the color and magnetic field was then calibrated, to create the color scale.

3. Results and Discussion

3. 1 Figures of merit for the MO imaging plates

Faraday rotation spectra of Bi2.5:NIG films prepared on glass substrates at annealing temperatures of 600–700 °C are shown in Fig. 3. Kerr rotation spectra of the same samples containing mirror layers are shown in Fig. 4. The thickness of the Bi2.5:NIG film was approximately 450 nm. Periodic structures are clearly observed in both figures, which arose due to interference of the light in the garnet layers. This indicated that the samples had optically smooth surfaces. The Faraday rotation spectra exhibited maxima at around 530 nm in wavelength, and were consistent with previous reports[15), 16)]. The Kerr rotation spectra exhibited maxima at 590–620 nm in wavelength, and their Kerr rotation angles were larger than the Faraday rotation angles at the same wavelength. However, the peaks in the Kerr rotation spectra at 530 nm were smaller than the Faraday rotation angles at the same wavelength, which was attributed to optical losses. The figure of merit of a magneto-optical material is usually defined as[19)-21)],

$$Q = 2\,|\theta_F| / \alpha = 2\,|\theta_F|\, t / ln\,(1/T) \quad \text{(deg.)}, \ (1)$$

where θ_F (deg./μm) is the Faraday rotation angle, $\alpha = t / ln(1/T)$ is the absorption coefficient, T is the transmittance, and t is the thickness of the MO film. However, equation (1) is unsuitable for determining the figure of merit of the current MO imaging plates. An effective rotation angle of the polarization plane should decrease with optical losses. This is due to optical absorption of the MO layer, and reflection at the substrate surface and at the interface between the substrate and MO film. Therefore, we define the figure of merit for the current MO imaging plates using the Kerr rotation angle θ_K, according to,

$$Q' = |\theta_K|\, t / ln(1/T) = |\theta_K'| / ln(1/T)\ \text{(deg.)}, \quad (2)$$

where θ_K (deg./μm) and θ_K' (deg.) is the Kerr rotation angle, T is the transmittance, and t is the thickness of the MO film.

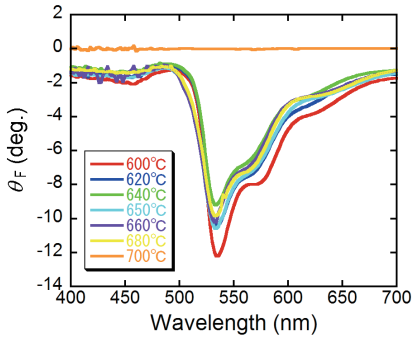

Fig. 3 Faraday rotation angles of MO imaging plates containing Bi2.5:NIG films annealed at 600–700 °C.

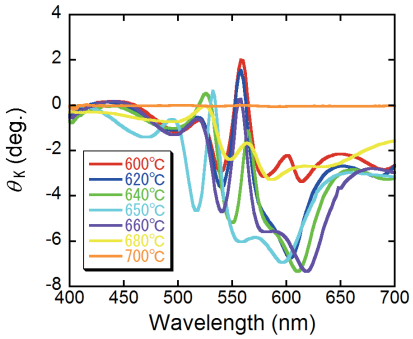

Fig. 4 Kerr rotation angles of MO imaging plates containing Bi2.5:NIG films annealed at 600–700 °C.

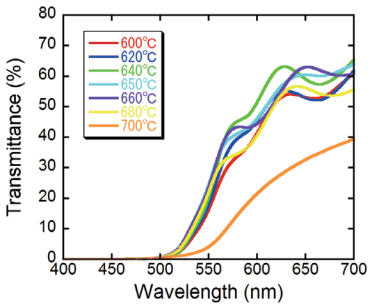

Fig. 5 Transmission spectra of MO imaging plates containing Bi2.5:NIG films annealed at 600–700 °C.

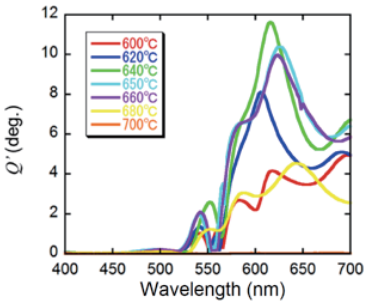

Fig. 6 MO figures of merit for MO imaging plates containing Bi2.5:NIG films crystallized at 600–700 °C.

Figures of merit Q' of the MO imaging plates as defined by equation (2) are shown in Fig. 6. Samples crystallized at 620–660 °C exhibited higher MO figures of merit at wavelengths of 580–650 nm. The highest figure of merit was obtained at a wavelength of 615 nm for the sample crystallized at 640 °C.

In MO imaging, in addition to the figure of merit of the MO imaging plates, the light source spectrum must also be considered. Spectra of the light sources used in the current study are shown in Fig. 7. A sharp peak at 450 nm and a broad peak at 525–625 nm were observed in the spectrum of the white LED, as shown in Fig. 7(a). Peaks at 530 and 600 nm were observed in the spectrum of the combined green and yellow LEDs, as shown in Fig. 7(b). Peaks at 470 and 600 nm were observed in the spectrum of the combined blue and yellow LEDs, as shown in Fig. 7(c). For MO imaging with the white LED, the Q' should be multiplied by the spectrum of the white LED, as shown in Fig. 8. Fig. 8 shows that under these conditions, the MO imaging plates could operate in the wavelength range of 570–650 nm, i.e. yellow-red.

3.2 MO color imaging

To develop MO color imaging to quantitatively determine the magnetic field, values of the magnetic field were calibrated for color. MO images and intensity spectra of a pole of the electromagnet were measured with a CMOS camera and spectrometer, respectively, using the experimental set up shown in Fig. 2. A MO imaging plate with a Bi2.5:NIG garnet film crystallized at 640 °C was used in this experiment, and the white LED was used as the light source. Fig. 9 shows intensity spectra of the reflected light, and MO images of the pole of the electromagnet, measured under applied magnetic fields of −1, 0, and +1 kOe. The colors were blue for −1 kOe, violet for 0 kOe, and yellow for +1 kOe. The intensity of the reflected light at a wavelength of 550–650 nm increased as the applied magnetic field increased in the positive direction. This corresponded to negative Kerr rotation. The profiles of the intensity spectra in Fig. 9 were consistent with the spectrum in Fig. 8. The intensity at 550 nm slightly increased as the applied magnetic field increased in the negative direction. A peak at 450 nm is observed in the spectrum in Fig. 9. This was derived from the peak of the white LED. The intensity of this peak was independent of the applied magnetic field, as the Q' was almost zero at the wavelength of 450 nm.

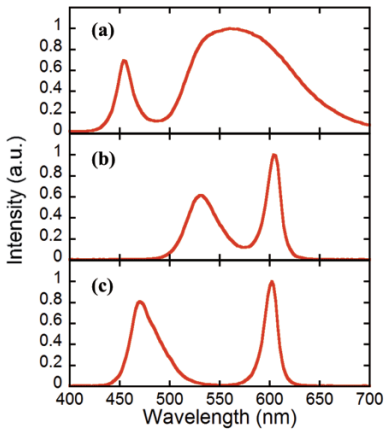

Fig. 7 Spectra of the (a) white LED, (b) combined green and yellow LEDs, and (c) combined blue and yellow LEDs, which were used as light sources.

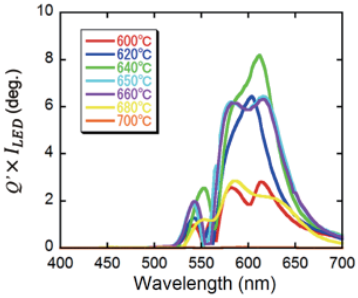

Fig. 8 Figures of merit of the MO imaging plates multiplied by the spectrum of the white LED.

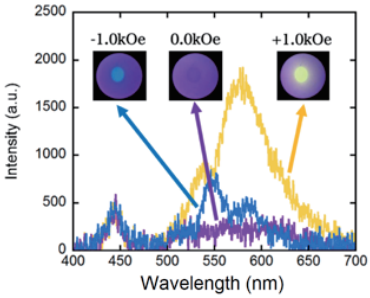

Fig. 9 Intensity spectra of the reflected light, and MO images of the pole of the electromagnet, measured under applied magnetic fields of −1, 0, and +1 kOe.

The result when using the combined green and yellow LEDs as the light source is shown in Fig. 10. Fig. 10(a) shows the Kerr rotation spectrum of a MO imaging plate containing the Bi2:NIG film used in this experiment. The Kerr rotation angles were +4 and −7 degrees at wavelengths of 530 and 595 nm, respectively. The Kerr rotation angle at 530 nm was larger than that of Bi2.5:NIG. This was because the transmittance at 530 nm of the MO imaging plate containing the Bi2:NIG film was higher. Peaks are observed at 530 and 600 nm in the intensity spectra in Fig. 10(b). These peaks increased asymmetrically with increasing applied magnetic field, as shown in Fig. 10(b). This resulted in the color becoming green at −1.0 kOe, dark green at 0.0 kOe, and yellow at +1.0 kOe. The asymmetric behavior of the intensities of these two peaks can be explained by the Kerr rotation spectrum in Fig. 10(a). The Kerr spectrum contained peaks at 530, 540, and 600 nm which are involved in this phenomenon. The sign of the Kerr rotation at 530 nm was opposite to those at 540 and 600 nm, and the angle of the analyzer was rotated −6° from the cross-polarized position. Therefore, the intensity at 530 nm decreased from −2 kOe to +0.5 kOe, and then increased. In contrast, the intensity at 600 nm increased from −0.5 kOe with applied magnetic field.

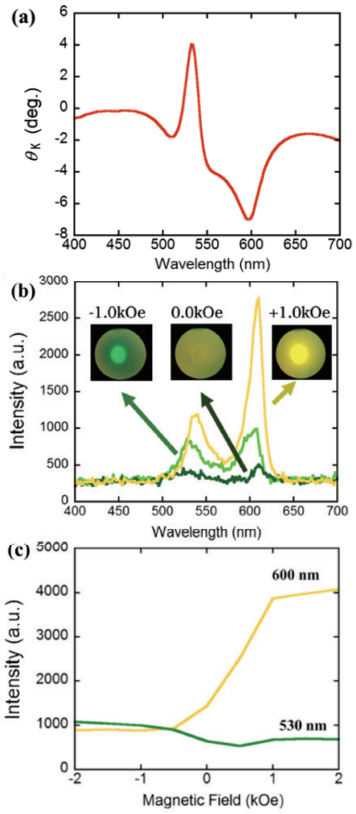

Fig. 10 (a) Kerr spectrum of the Bi2:NIG film on the glass substrate, (b) intensity spectra of the reflected light, and MO images of the pole of an electromagnet measured, at −1, 0, and +1 kOe, and (c) dependence of light intensity on applied magnetic field, at wavelengths of 530 and 600 nm.

Fig. 11 shows the MO images of the pole of an electromagnet measured using the white LED, combined green and yellow LEDs, and combined blue and yellow LEDs, as light sources. The colors changed from blue to yellow, from green to yellow, and, from blue to red, respectively, with changing magnetic field. This constituted color scales corresponding to the magnetic field. Quantitative color values were obtained as RGB values, which were deduced from the measured spectra. Values for the xy colorimetric system were then obtained from the RGB values. The three curves corresponding to the data in Fig. 11 are plotted in the chromaticity diagram (CIE1931) in Fig. 12. The magnetic field values were quantitatively evaluated with colors.

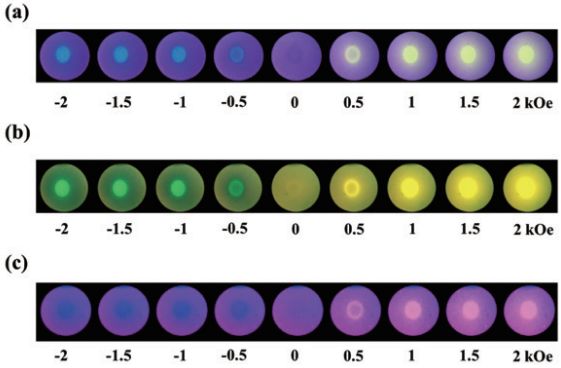

Fig. 11 MO images of the pole of an electromagnet, in which the light source was (a) a white LED, (b) combined green and yellow LEDs, and (c) combined blue and yellow LEDs.

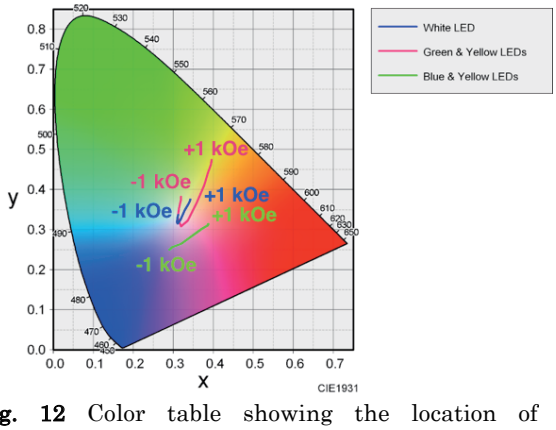

Fig. 12 Color table showing the location of experimentally-obtained data using the white LED, green and yellow LEDs, and blue and yellow LEDs as light sources.

Quantitative MO color imaging using the white LED is demonstrated in Fig. 13. Connected spherical neodymium magnets were measured as a sample, which is shown in Fig. 13(a). A color scale prepared using the procedure described above is shown together with an MO image in Fig. 13(b). The MO image shows the quantitative distribution of the magnetic fields directly above the magnets. South (S) and north (N) magnetic poles are indicated by blue and yellow, respectively, and

zero points are indicated by violet. The magnetic fields could also be expressed in RGB values.

Kerr rotation spectra of various garnet films with different film compositions and substrate types are shown in Fig. 14. The spectral profiles strongly depended on the film composition and substrate material. However, the spectral profiles could potentially be modeled by optical simulations, if the optical constants including the permittivity tensors are known[22].

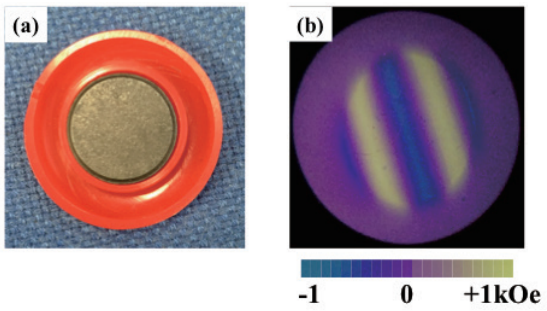

Fig. 13 (a) Digital photograph of spherical magnets, and (b) corresponding MO color image.

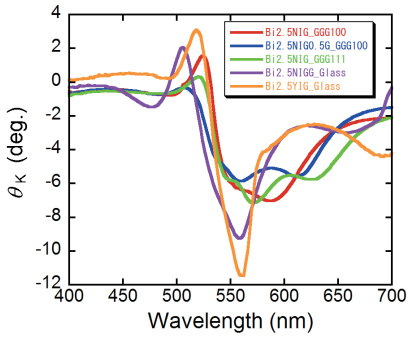

Fig. 14 Kerr rotation spectra of various garnet films with different film compositions and substrate types.

4. Conclusions

We have developed a MO imaging plate containing Bi2:NIG and Bi2.5:NIG films for MO color imaging. The MO figure of merit for the MO imaging plates defined in this study accurately represents their MO properties with respect to MO imaging. The MO imaging plates using Bi2.5:NIG exhibited a high MO figure of merit in the 570–650 nm wavelength range. The color varied from blue to yellow, as the magnetic field changed from −2 to +2 kOe, when using a white LED. The color changed from green to yellow, or from blue to red, when combined green and yellow LEDs and combined blue and yellow LEDs were used as light sources, respectively. A color scale indicating values of the magnetic field was obtained, along with a MO color image of a ferrite magnet. These collectively displayed the intensity and pattern of the magnetic field in color.

Acknowledgement

The authors thank Dr. Yongfu Cai for technical assistance with experiments.

References

1) S. Gotoh, N. Koshizuka, M. Yoshida, M. Murakami, and S. Tanaka: *Jpn. J. Appl. Phys.*, **29,** L1083 (1990).
2) M. V. Indenbom, N. N. Kolesnikov, M. P. Kulakov, I. G. Naumenko, V. I. Nikitenko, A. A. Polyanskii, N. F. Vershinin, and V. K. Vlasko-Vlasov: *Physica C*, **166,** 486 (1990).
3) T. H. Johansen, and D. V. Shantsev: *Magneto-Optical Imaging, NATO Science Series II Mathematics, Physics, and Chemistry*, (Kluwer Academic, Dordrecht 2004) pp.1-10.
4) Ch. Joose, A. Forkl, R. Wrthmann, H.-U. Hbermeier, B. Leibold, and H. Kronmüller: *Physica C*, **266**, 235 (1996).
5) Ch. Joose, J. Albrecht, H. Kuhn, S. Leonhardt, and H. Kronmüller: *Rep. Prog. Phys.*, **65,** 651 (2002).
6) T. Ishibashi, Z. Kuang, S. Yufune, T. Kawata, M. Oda, T. Tani, Y. Iimura, K. Sato, Y. Konishi, K. Akahane, X. Zhao, and T. Hasegawa: *J. Appl. Phys.*, **100**, 093903 (2006).
7) L. A. Dorosinskii, M. V. Indenbom, V. I. Nikitenko, Yu. A. Ossip'yan, A. A. Polyanskii, and V. K. Vlasko-Vlasov: *Physica C*, **203**, 149 (1992).
8) T. Ishibashi, G. Lou, A. Meguro, T. Hashinaka, M. Sasaki, and T. Nishi: *Sensors and Materials*, **27**, 965 (2015).
9) W. C. Patterson, N. Garraud, E. E. Shorman, and D. P. Arnold: *Rev. Sci. Instrum.*, **86,** 094704 (2015).
10) M. Takahashi, K. Kawasaki, H. Ohba, T. Ikenaga, H. Ota, T. Orikasa, N. Adachi, K. Ishiyama, and K. I. Arai: *J. Appl. Phys.*, **107**, 09E711 (2010).
11) N. Adachi, D. Uematsu, T. Ota, M. Takahashi, K. Ishiyama, K. Kawasaki, H. Ota, K. Arai, S. Fujisawa, S. Okubo, and H. Ohta: *IEEE Trans. Magn.*, **46**, 1986 (2010).
12) K. Iida, N. Kawamae, S. Hoshi, T. Machi, T. Kono, J. Yoshioka-Kato, N. Chikumoto, N. Koshizuka, N. Adachi, and T. Okuda: *Jpn. J. Appl. Phys.*, **44**, 1734 (2005).
13) H. Lee, T. Kim, S. Kim, Y. Yoon, S. Kim, A. Babajanyan, T. Ishibashi, B. Friedman, and K. Lee: *J. Magn. Magn. Mater.*, **322**, 2722 (2010).
14) T. Kono, T. Machi, N. Chikumoto, K. Nakao, N. Koshizuka, N. Adachi, and T. Okuda: *J. Magn. Soc. Jpn.*, **30**, 600 (2006).
15) T. Yoshida, K. Oishi, T. Nishi, and T. Ishibashi: *EPJ Web Conf.*, **75**, 05009 (2014).
16) G. Lou, T. Yoshida, and T. Ishibashi: *J. Appl. Phys.*, **117**, 17A749 (2015).
17) T. Ishibashi, T. Yoshida, T. Kobayashi, S. Ikehara, and T. Nishi: *J. Appl. Phys.*, **113**, 17A926 (2013).
18) T. Kosaka, M. Naganuma, M. Aoyagi, T. Kobayasi, S. Niratisairak, T. Nomura, and T. Ishibashi: *J. Magn. Soc. Jpn.*, **35**, 194 (2011).
19) P. Hansen, K. Witter, and W. Tolksdorf: *Phys. Rev. B*, **27**, 6608 (1983).
20) A. M. Grishin, S. I. Khartsev, and S. Bonetti: *Appl. Phys. Lett.*, **88**, 242504 (2006).
21) S. Kang, S. Yin, V. Adyam, Q. Li, and Y. Zhu: *IEEE Trans. Magn.*, **43**, 3656 (2007).
22) E. Jesenska, T. Yoshida, K. Shinozaki, T. Ishibashi, L. Beran, M. Zahradnik, R. Antos, M. Kučera, and M. Veis: *Optical Materials Express*, **6**, 1986 (2016).

Received Oct. 11, 2016; Accepted Jan. 10, 2017

J. Magn. Soc. Jpn., **41**, 34-40 (2017)

<Paper>

Reduction of vibration amplitude in vibration-type electricity generator using magnetic wire

Akitoshi Takebuchi, Tsutomu Yamada, and Yasushi Takemura

Department of Electrical and Computer Engineering, Yokohama National Univ.,

79-5 Tokiwadai, Hodogaya-ku, Yokohama 240-8501, Japan

A fast magnetization reversal accompanied by a large Barkhausen jump in a magnetic wire is utilized in speed sensors, rotation sensors, and other applications. This magnetization reversal induces a pulse voltage in a pick-up coil, which can also be applied for electricity generation as an energy-harvesting element. Dependence of the output voltage on the position of the pick-up coil indicated a fast magnetization reversal by a domain wall propagation. An excitation method for a vibration-type electricity-generating element using a single magnet was optimized by changing the magnet size. The output voltage obtained from the FeCoV wire depended on the amplitude of vibration of an excitation magnet. In order to minimize the vibration amplitude of an excitation magnet required for generating the output voltage, a field distribution from magnets of various sizes was calculated. It was found that just a 0.6 mm-movement of an NdFeB magnet was sufficient to generate the output voltage.

Keywords: magnetic sensor, large Barkhausen jump, FeCoV wire, vibration-type electricity generator, energy harvesting

1. Introduction

A fast magnetization reversal in magnetic wires with bistable states induces a pulse voltage in a pick-up coil. This fast magnetization reversal is accompanied by a large Barkhausen jump, which is known as the Wiegand effect[1]. In this study, a twisted FeCoV wire, one of the optimum materials yielding this effect, was used. A magnetic sensor that uses the Wiegand effect has certain advantages: no external power supply is necessary, and the amplitude of the pulse voltage does not depend on the frequency of an applied magnetic field. This phenomenon has been used in various sensor applications, including speed sensor and rotation sensor[2,3]. In this paper, a vibration-type energy-generating element using the Wiegand effect is reported.

Power generation by environmental vibration is a promising technique for energy harvesting. Vibration-type energy-generating elements, which convert vibration to electricity, mostly have their own eigenfrequency or resonant frequency[4,5]. Vibration at frequency ranges other than specific frequency results in a drastic decrease in electricity generation efficiency[5]. Electricity generation from a vibration-type energy-harvesting element using a FeCoV wire was studied in this paper. The output pulse voltage obtained from the FeCoV wire is expected to be independent of the vibration frequency.

2. Structure of electricity generator

2.1 FeCoV wire

A FeCoV ($Fe_{0.4}Co_{0.5}V_{0.1}$) wire of 0.25 mm diameter and 20 mm length was used in this study. When a torsion stress is applied to the wire, the outer shell near the surface becomes magnetically soft. After releasing the stress, the wire exhibits coercive forces of 20 Oe in the soft layer and 80 Oe in the hard core. Details on magnetic properties of twisted FeCoV wires, including torsion stress dependence, have been reported by Abe *et al.*[6,7]. The magnetic wire shows a uniaxial magnetic anisotropy along its length. The magnetization alignment of the soft layer and the hard core can be in either a parallel state or an antiparallel state, as shown in Figs. 1(a) and (b), respectively.

Figure 2 shows a typical hysteresis loop of the FeCoV wire used in this study, which is essentially the same as that reported in Ref, 6) and 7). The magnetization direction of the soft layer and that of the hard core

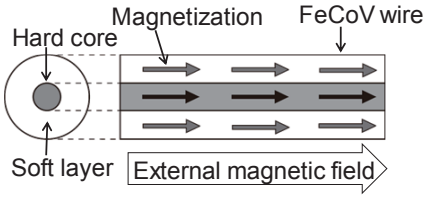

(a) Parallel alignment.

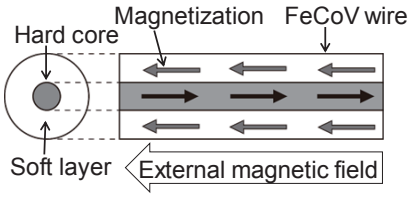

(b) Antiparallel alignment.

Fig. 1 Schematic diagrams of magnetic structure of FeCoV wire with (a) parallel and (b) antiparallel alignments of soft layer and hard core.

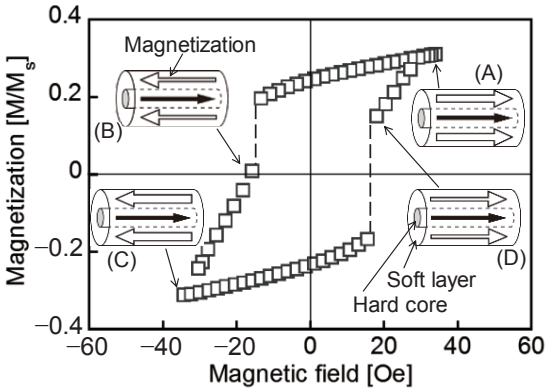

Fig. 2 The measured hysteresis loop of FeCoV wire. A static magnetic field up to 35 Oe was applied.

exhibit a parallel state when an external magnetic field larger than 35 Oe was applied along its length, as indicated by (A) in the figure. When a magnetic field with a negative direction reaches −20 Oe, the magnetization of the soft layer is reversed rapidly as indicated by (B). This magnetization reversal, called the Wiegand effect, is due to a fast domain wall propagation. Owing to this magnetization reversal of the soft layer from the parallel state to the antiparallel state, a pulse voltage is induced in a pick-up coil wound around the wire. The magnetization of the soft layer along the left direction is increased by increasing the externally applied magnetic field of the negative direction from −20 Oe (B) to −35 Oe (C). The pulse voltage of the opposite direction is obtained during the magnetization reversal from the antiparallel state (C) to parallel state (D). Within the applied field intensity of ±35 Oe, the magnetization of the hard core is not reversed.

2.2 Vibration of a magnet for electricity generator

A pair of excitation magnets has been conventionally used for repeating the generations of the positive and negative pulse output voltages induced from the wire. In this study, only a single magnet[8] was used to apply a magnetic field of both positive and negative directions to the wire as shown in Fig. 3. This method is advantageous for a vibration-type element in terms of the device structure.

3. Experiment

3.1 Dependence on the position of the excitation magnet

Two pick-up coils of 2 mm length and 50 turns each indicated by Coil 1 and Coil 2 in Fig. 4(a) were wound around the FeCoV wire (diameter: 0.25 mm, length: 20 mm). The output voltage induced in these pickups was measured by changing the position of the excitation NdFeB magnet of 4×4×12 mm^3 in dimension, where the length of the magnet (12 mm) is along its magnetization. The underline below the length denotes the magnetization direction of the magnet. The magnet was

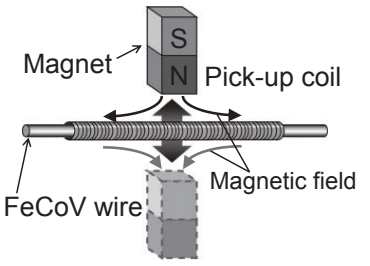

Fig. 3 Configuration of magnetic wire, magnet, and pick-up coil for electricity generator.

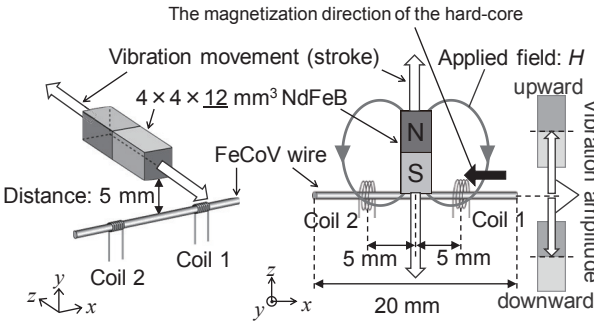

(a) Configuration for measurement of induced voltage.

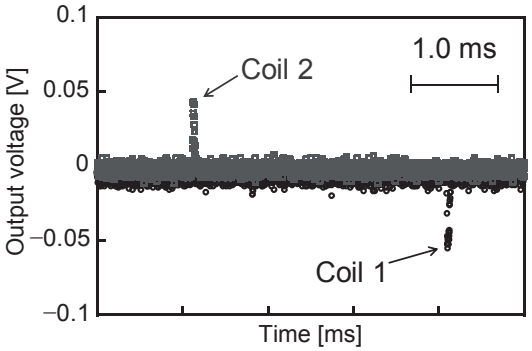

(b) Output voltage measured by pick-up coils.

Fig. 4 Configuration of FeCoV wire, pick-up coils, and excitation magnet (a), and waveforms of pulse voltage induced in pick-up coils (b). The excitation magnet was vibrated horizontally at the center of the wire.

vibrated at the center and the end of the wire as shown in Figs. 4(a) and 5(a), respectively. The magnet was vibrated as slow as at 1 Hz. It was confirmed that the output voltage was independent of the vibration frequency.

A vibration amplitude is defined as a length of movement of the vibrated magnet. Each upward or downward movement of the magnet is described as "stroke" in this paper.

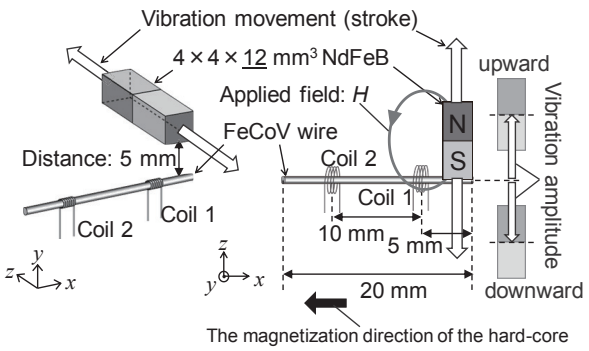

(a) Configuration for measurement of induced voltage.

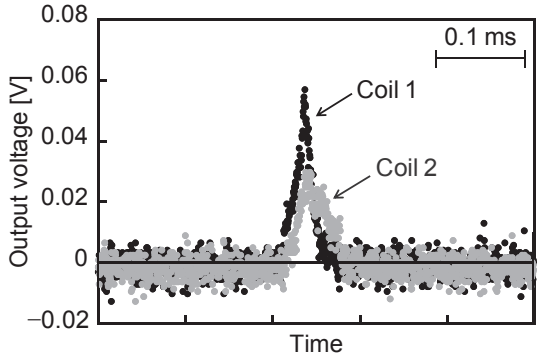

(b) Output voltage measured by pick-up coils.

Fig. 5 Configuration of FeCoV wire, pick-up coils, and excitation magnet (a), and waveforms of pulse voltage induced in pick-up coils (b). The excitation magnet was vibrated horizontally at the end of the wire.

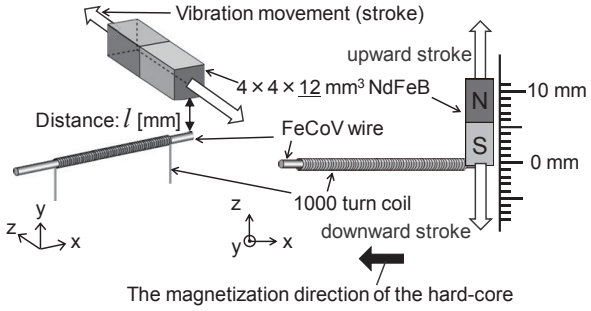

(a) Configuration for measurement of induced voltage.

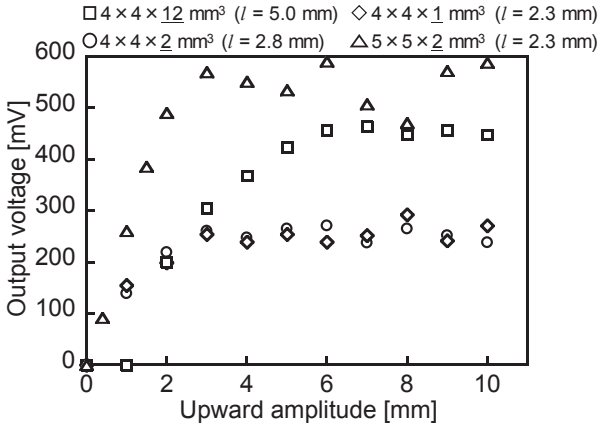

(b) Output voltage measured by pick-up coils.

Fig. 6 Configuration of FeCoV wire, pick-up coil, and excitation magnet (a), and induced output voltages obtained by using various sizes of NdFeB magnets plotted as a function of amplitude of upward stroke.

3.2 Dependence on the vibration amplitude of the exciting magnet

The excitation magnet positioned at the end of FeCoV wire (diameter: 0.25 mm, length: 20 mm) was vibrated along the perpendicular direction to the wire, as shown in Fig. 6(a). The output voltages induced in a pick-up coil (1,000 turns and 20 mm length) wound around the wire was measured. The dependence of the output pulse voltage on the vibration amplitude of the magnet was evaluated for various sizes of the excitation magnet.

4. Results and Discussion

4.1 Position of exciting magnet and induced pulse voltage

Figure 4(b) shows the typical waveforms of the pulse voltage induced in the pick-up coils of Coil 1 and 2. These coils were positioned at the right and left sides, 5 mm from the wire center, respectively, as shown in Fig. 4(a). When the excitation magnet was vibrated along the perpendicular direction to the wire, the positive and negative output voltages were induced in Coils 1 and 2, respectively. The amplitude of these two output voltages is almost equivalent. This is because the magnetization reversal initiated from the center of the wire, and the magnetization is reversed from the center to both ends of the wire as well as the propagation of the domain wall. On the other hand, when the magnet was vibrated at the end of the wire, the positive output voltages with different amplitudes were induced in Coils 1 and 2, as shown in Figs. 5(a) and 5(b), respectively. This result shows that the magnetization reversal is accompanied by a single domain-wall propagation. The time difference between these two positive pulse voltages agrees with the calculation performed using the distance of the coils and the velocity of the domain wall propagation, which was 500 m/s[9]. The amplitude of the pulse voltage induced in Coil 2 was smaller than that induced in Coil 1. This is because of the energy loss of the domain wall propagation and the smaller amount of reversed magnetization. The intensity of an applied magnetic field from the magnet positioned at the end of the wire was lesser at the position of Coil 2 than it was at that of Coil 1. The full width at half maximum of the pulse voltage induced in Coil 2 was larger than that in Coil 1, which was due to the scattering of the domain

Table 1 Upward amplitudes for their minimum value to obtain the pulse voltage and for giving the saturated voltage, and downward amplitude for generating pulse voltage.

	$4 \times 4 \times \underline{12}$ mm^3 (l = 5 mm)	$4 \times 4 \times \underline{2}$ mm^3 (l = 2.8 mm)	$4 \times 4 \times \underline{1}$ mm^3 (l = 2.3 mm)	$5 \times 5 \times \underline{2}$ mm^3 (l = 2.3 mm)
Minimum upward amplitude [mm]	2	1	1	0.4
Upward amplitude for saturating output [mm]	6	2	3	3
Downward amplitude for pulse generation [mm]	−1	−0.4	−0.5	−0.2

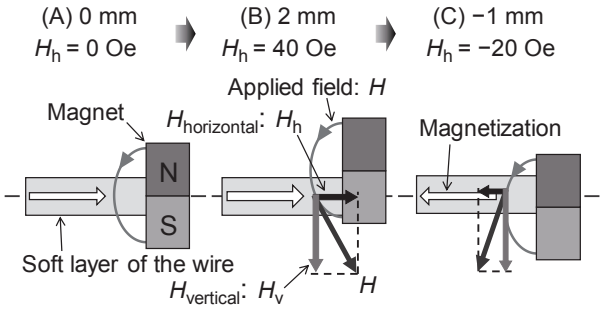

(a) In the case of upward amplitude is small.

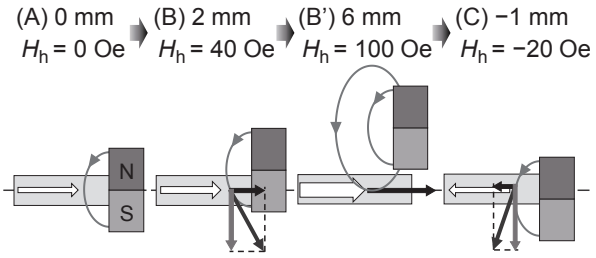

(b) In the case of upward amplitude is large.

Fig. 7 Schematics of positions of the excitation magnet and its magnetic field distribution. A component of the magnetic field along the wire direction is denoted as H_h.

wall propagation at the impurities and defects in the wire.

4.2 Dependence on stroke amplitude of the exciting magnet

Dependence of the output voltage on the vibration amplitude of the excitation magnet is shown in Fig. 6(b). Figure 6(a) illustrates the initial position of the excitation magnet. The vertical distance, l, between the wire and the magnet was 5 mm. The center of the magnet was at 0 mm at the initial position. Then, the magnet was moved upwards as indicated by (A) to (B) in Fig. 7(a). Only the magnetization of the soft layer was shown in all illustrations in Fig. 7. The upward amplitude is 2 mm in case of (B). At this position of the excitation NdFeB magnet of $4 \times 4 \times \underline{12}$ mm^3 in dimension, the intensity of the applied magnetic field along the wire direction, noted as H_h in (B) of Fig. 7(b), was 40 Oe.

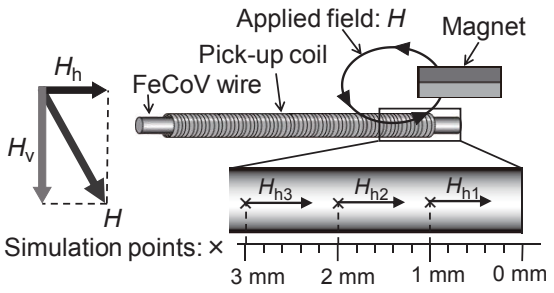

Fig. 8 Schematics indicating H_{h1}, H_{h2}, and H_{h3}, components of a magnetic field from the FeCoV wire along the wire direction. They are the magnetic fields at 1 mm, 2 mm, and 3 mm from the end of the wire.

This field assures the magnetization direction of the soft layer with a positive direction (right side direction in the figure). When the magnet was moved downward from (B) to (C), the pulse voltage was induced in the pick-up coil. The position of the excitation magnet for inducing the pulse voltage was reproducible at −1 mm. H_h was −20 Oe at this position, which agreed with the switching field of the soft layer. This position was independent of the amplitude of the upward stroke of the magnet[10].

Open squares in Fig. 6(b) indicate the output voltage induced at the magnet position of −1 mm as a function of the amplitude of upward stroke of the magnet with $4 \times 4 \times \underline{12}$ mm^3 in dimension. It was found that the pulse voltage was obtained if the upward amplitude was 2 mm or larger. The pulse voltage increased with an increase in the upward amplitude, but saturated at 6 mm. The increase and saturation was due to a larger volume of the reversed magnetization of the soft layer and the magnetization saturation of the soft layer, respectively.

4.3 Dependence on the magnet dimensions

In order to reduce a vibration amplitude in this electricity-generating element, the output voltage was measured by changing the length of the excitation magnet. The magnets of $4 \times 4 \times \underline{12}$ mm^3 (l = 5.0 mm), $4 \times 4 \times \underline{2}$ mm^3 (l = 2.8 mm) and $4 \times 4 \times \underline{1}$ mm^3 (l = 2.3 mm) for each dimension were used. The vertical distance between the wire and the magnet, l, was adjusted by

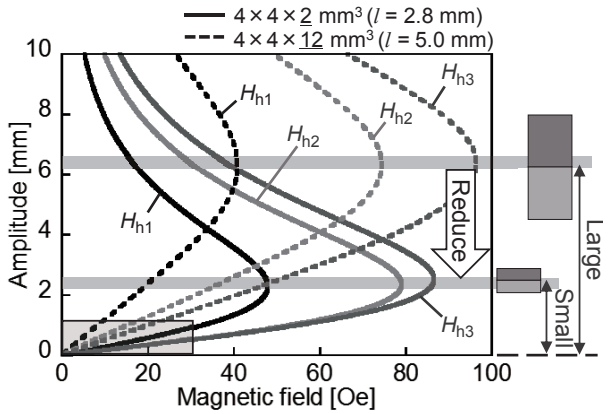

(a) Simulated values of the field intensity.

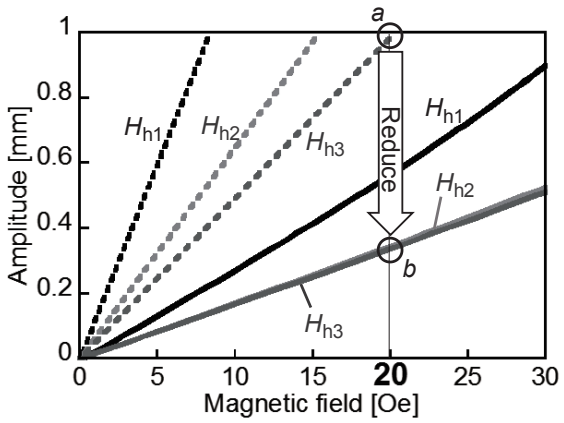

(b) Magnified images of (a) at low magnetic field.

Fig. 9 Magnetic field intensity of component of wire direction, H_h, from NdFeB magnets of 4 × 4 × 12 mm³ and 4 × 4 × 2 mm³ in dimension calculated as a function of the position of the magnet (equivalent to upward and downward amplitudes).

considering the magnet size. The induced pulse voltages measured using these magnets are plotted as a function of the amplitude of the upward stroke in Fig. 6. The magnet of 4×4×2 mm³ could reduce the minimum value of upward amplitude for generating a pulse voltage down to 1.0 mm. The pulse voltage was induced when the position of the magnet was −0.4 mm. This result shows that electricity can be generated by a vibration of 1.4 mm (upward 1.0 mm + downward −0.4 mm) of the magnet.

In order to understand this dependence on magnet size, the magnetic field distribution was calculated using a commercial software (JMAG distributed by JSOL Corporation). The magnetic field intensity along the wire directions, H_{h1}, H_{h2} and H_{h3}, were calculated, which are the magnetic fields at 1 mm, 2 mm and 3 mm from the wire end, respectively, as shown in Fig. 8. As the FeCoV wire exhibits strong uniaxial anisotropy

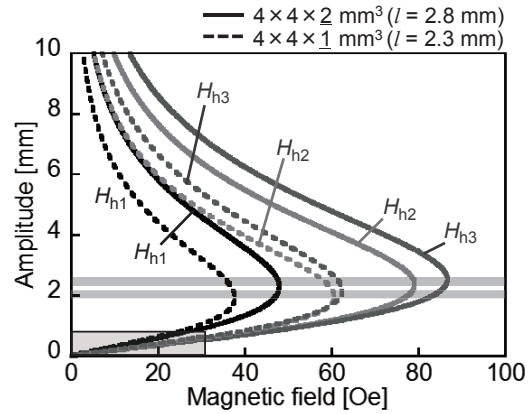

(a) Simulated values of the field intensity.

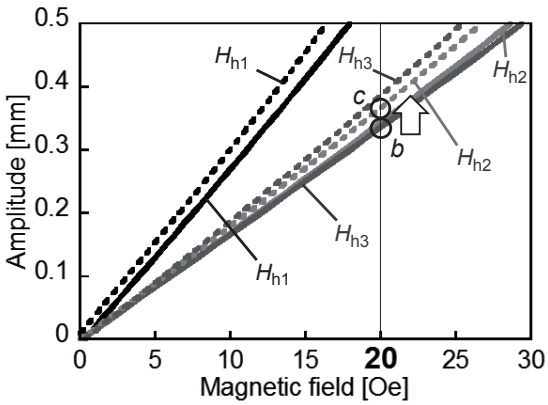

(b) Magnified images of (a) at low magnetic field.

Fig. 10 Magnetic field intensity of component of wire direction, H_h, from NdFeB magnets of 4 × 4 × 2 mm³ and 4 × 4 × 1 mm³ in dimension calculated as a function of the position of the magnet (equivalent to upward and downward amplitudes).

along the wire direction, the wire-direction component of the applied magnetic field is essential to discuss the magnetization reversal of the wire. The numerical analysis based on the field intensities of H_{h1}, H_{h2} and H_{h3} was sufficient to discuss the experimental results, as described afterwards.

Figure 9 shows the simulated values of the field intensity of the 4×4×12 mm³ and the 4×4×2 mm³ magnets as a function of the position of the magnet while vibrating in the upward/downward directions. The position of the magnets at of 6 mm and 2 mm for giving the maximum magnetic field intensities of H_{h1}, H_{h2} and H_{h3} from the 4×4×12 mm³ and the 4×4×2 mm³ dimensions, respectively, as shown by gray lines in Fig. 9(a) agreed with the upward amplitudes at which the increase in output voltage was saturated for each magnet.

Figure 9(b) is a magnified image of Fig. 9(a) for the

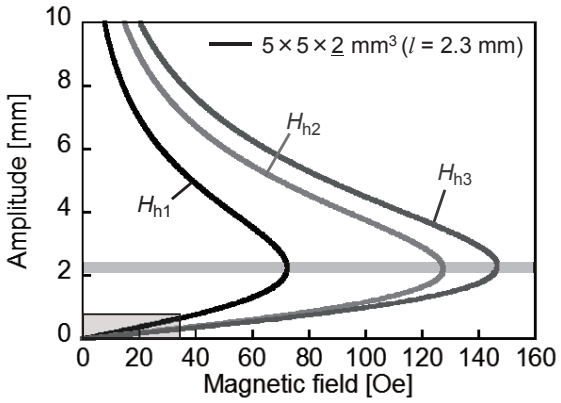

(a) Simulated values of the field intensity.

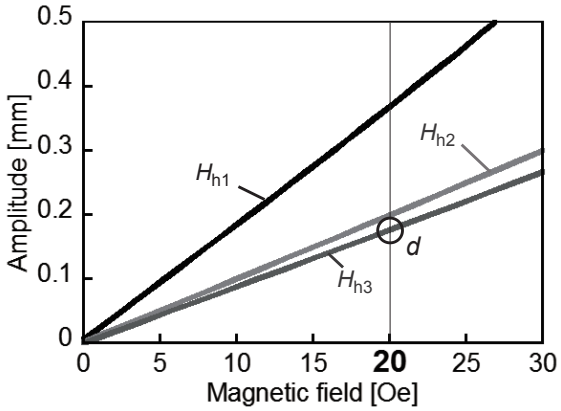

(b) Magnified images of (a) at low magnetic field.

Fig. 11 Magnetic field intensity of component of wire direction, H_h, from NdFeB magnet of 5 × 5 × 2 mm³ in dimension calculated as a function of the position of the magnet (equivalent to upward and downward amplitudes).

magnetic field range of 0–30 Oe. The positions for the applied magnetic field of 20 Oe, which is a switching field of soft layer, are calculated to 1.0 mm and 0.4 mm for the 4×4×12 mm³ and 4×4×2 mm³ magnets, respectively. These positions noted by circles (a) and (b) in the figure agree with the downward amplitudes of the magnet for generating the pulse voltage due to the magnetization reversal of the soft layer. Table 1 summarizes these specific upward and downward amplitudes theoretically supported by the simulation of the magnetic field distribution.

Figure 6(b) also shows the output voltage dependence on the upward amplitude of an 4×4×1 mm³ magnet. The experimental results indicate that the output properties using 4×4×2 mm³ and 4×4×1 mm³ magnets are similar. This is also confirmed by the calculated results shown by Fig. 10(a) and 10(b). The positions of the magnets for the maximum magnetic field and for applying 20 Oe were not different between in the two magnets, as indicated by circles (b) and (c) in Fig. 10(b).

A magnetic field intensity of H_{h1} is smaller than those of H_{h2} and H_{h3} as shown in Figs. 9 and 10. This is because that the direction of the magnetic field at 1 mm from the edge of the wire is close to perpendicular to the wire direction, and that H_{h1}, the wire-direction component of the applied magnetic field, is small. The magnetization reversal of the wire is initiated by the applied field of H_{h2} and H_{h3}.

Finally, the output property with the optimized magnet dimension and distance between the wire and the magnet is reported. Figure 6(b) shows the output voltage measured using an NdFeB magnet of 5×5×2 mm³ (l = 2.3 mm) in dimension. Figure 11 shows the simulated values of the field intensity of this magnet. The output voltage was as large as 600 mV. The minimum value of the upward amplitude for generating pulse voltage was as small as 0.4 mm. The pulse voltage was induced when the downward amplitude was 0.2 mm. This agreed with the calculated amplitude for reversing the magnetization of the soft layer, indicated by circle (d) in Fig. 11(b). It was found that the electricity generation can be obtained by a vibration of 0.6 mm (upward 0.4 mm + downward −0.2 mm) of the magnet. These values for upward and downward amplitudes, which are summarized in Table 1, are mostly consistent with the simulated result of a magnetic field distribution, as shown in Figs. 9, 10 and 11.

5. Conclusion

This paper proposes a vibration-type electricity generator using a FeCoV wire. The pulse voltage was induced in a pick-up coil wound around the wire by vibrating an excitation magnet. The induced output voltage was attributed to a fast magnetization reversal of the wire known as the Wiegand effect. Dependence of the output voltage on the position of a pick-up coil indicated a fast magnetization reversal by a domain wall propagation. An excitation method using a single magnet for a vibration-type electricity-generating element was optimized by changing the size of the excitation magnet. The minimum amplitude of vibration of the excitation magnet required to obtain the output voltage strongly depended on the dimension of the magnets, which agreed well with the calculated results of a field distribution from the magnets. It was found that even a 0.6 mm-movement of the NdFeB magnet of 5×5×2 mm³ in dimension could generate a pulse voltage.

Acknowledgment The authors would like to express their gratitude to Nikkoshi Co., Ltd, Japan for supplying FeCoV wires.

References

1) J. R. Wiegand and M. Velinsky: U.S. Patent #3,820,090 (1974).
2) R. Malmhall, K. Mohri, F. B. Humphrey, T. Manabe, H.

Kawamura, J. Yamasaki and I. Ogasawara, *IEEE Trans. Magn.*, **23**, 3242 (1987).
3) M. Vázquez, C. Gómez- Polo, D.-X. Chen and A. Hernando, *IEEE Trans. Magn.*, **30**, 907 (1994).
4) A. Moure, M.A. Izquierdo Rodríguez, S. Hernández Rueda, A. Gonzalo, F. Rubio-Marcos, D. Urquiza Cuadros, A. Pérez-Lepe, J.F. Fernández, Energ. *Convers. Manage.*, **112**, 246 (2016).
5) V. Ostasevicius, V. Markevicius, V. Jurenas, M. Zilys, M. Cepenas, L. Kizauskiene, V. Gyliene, *Sensor Actuat. A-Phys.*, **233**, 310 (2015).
6) S. Abe and A. Matsushita, *IEEE Trans. Magn.*, **31**, 3152 (1995) .
7) S. Abe, A. Matsushita, and M. Naoe, *IEEE Trans. Magn.*, **33**, 3916 (1997).
8) T. Kohara, T. Yamada, S. Abe, S. Kohno, F. Kaneko and Y. Takemura, *J. Appl. Phys.*, **109**, 07E531-1 (2011).
9) H. Tanaka, T. Yamada, Y. Takamura, S. Abe, S. Kohno and H. Nakamura, *IEEE Trans. Magn.*, **43**, 2397 (2007).
10) A. Takebuchi, N. Kameda, T. Yamada, Y. Takemura, 2016 Joint MMM-Intermag Conference, DJ-02, San Diego, Jan, 2016.

Received Oct. 10, 2016; Revised Nov. 29, 2016; Accepted Dec. 22, 2016

J. Magn. Soc. Jpn., **41**, 41-45 (2017)

<Paper>

Automatic component selection for noise reduction in magnetocardiograph based on independent component analysis

M. Iwai, K. Kobayashi, M. Yoshizawa, Y. Uchikawa*, and F. M. Bui**

Iwate University, *4-3-5 Ueda, Morioka, Iwate 020-8551, Japan*

*Tokyo Denki University, *Ishizaka Hatoyama, Hiki-gun, Saitama 350-0394, Japan*

** University of Saskatchewan, *57 Campus Drive, Saskatoon, SK S7N 5A9, Canada*

Magnetocardiogram (MCG) measurement systems require noise reduction, because MCG signals are extremely small compared to environmental magnetic noise. We investigate the efficacy of a novel noise-reduction method, based on an independent component analysis (ICA). The proposed noise reduction method requires a component selection process to distinguish signal from noise. A major challenge in applying ICA-based noise reduction method is the selection of suitable parameters, which in practice is often performed manually with rather subjective parameter choices. To address this issue, we proposed a component selection method that can be performed quantitatively and automatically. The proposed method is based on the peak values of the autocorrelation function and helps distinguish the independent components of the MCG signals from the noise using an appropriate threshold. By using the proposed method, we obtain output signal-to-noise ratios (SNRs) of 33.98 dB, 19.17 dB, and 13.56 dB, corresponding to input SNRs for the simulated data at respectively 0 dB, -10 dB, and -20 dB, after noise reduction. The results show that the proposed method exhibits remarkable promise in extracting a noise-mitigated MCG signal for a wide range of SNRs.

Key words: magnetocardiogram, principal component analysis, independent component analysis, autocorrelation function, component selection

1. Introduction

In recent years, magnetocardiogram (MCG) has become increasingly relevant for clinical research, due to its potential to detect early stages of heart disease. However, it is difficult to assess heart activity precisely without some form of noise reduction, because MCG measurements are extremely small compared to environmental magnetic noise.

A possible solution that can suppress the noise is the use of a digital signal processing (DSP) method. The finite impulse response (FIR) filter is a well-known method in reducing noise via DSP. However, FIR filters have various issues such as distorted waveforms, generation of phase differences, and reduced signal peaks.

Hence, a noise reduction method using an independent component analysis (ICA) is considered. This method has the ability to distinguish between independent components, whether those are MCG signals or noise. Component selection is important for accuracy of noise reduction. There are two steps involved in selecting the independent components that represent MCG signals in an inverse process:

1. Distinguish between independent components separated using the ICA, whether those are MCG signals or noise.
2. Select the independent components that are determined to be MCG signal components.

In many cases, these processes have been performed by individual subjective judgment from a waveform of independent components. Hence, the results of this process differ from person to person. The process cannot be performed automatically and quantitatively, because there are no appropriate parameters that can distinguish the independent components between MCG signals and noise using measurement data. In addition, the component selection process has not been discussed in detail up until now[1)-6)].

Therefore, we propose a new component selection method that can be used to reduce noise automatically and quantitatively by using measurement data. We have considered the proposed method can distinguish between the independent components of MCG signals and noise. We compare the proposed method with other component selection methods such as subjective judgment from the waveforms of independent components and the highest noise reduction accuracy.

2. Noise reduction method using the ICA

2.1 Noise reduction procedure

First, we explain the process of the noise reduction method using the ICA as follows[7)-8)]:

1. Apply principal component analysis (PCA) to measurement data for whitening.
2. Perform dimensional contraction to the whitening data (principal components) for eliminating unnecessary information and amount of calculation.
3. Apply the ICA to the whitening data for separating independent components as source signals (MCG signals, noise, or both).
4. Distinguish the independent components between MCG signals and noise, and select the independent components that represent MCG signals.

5. Apply an inverse process to reconstruct measurement data using the selected independent components. This process uses inverse matrices calculated from each separating matrix produced during the ICA and PCA processes.

After completing these processes, a noise-reduced MCG signal is obtained. Accuracy of the noise reduction depends largely on the selected components. Therefore, the focus should be on the component selection step so that the process can be performed automatically and quantitatively.

2.2 Independent component analysis (ICA)

The ICA is a method designed to separate measurement data into independent components, which represent the source signals. ICA is performed based on statistical independence, and the difference between various ICA algorithms lies in the method of obtaining statistical independence. Independent components are statistically independent from each other. The measurement data model can be expressed in the ICA algorithm as

$$\boldsymbol{X} = \boldsymbol{AS} \cdots (1)$$

where matrix **X** is the measurement data, matrix **A** is the mixing matrix, and matrix **S** contains the source signals. Using this model, we treated the noise as one of the source signals. In this flow, **X** is replaced with a matrix that represents whitening and dimensional contraction through PCA. The separating data model can be expressed as

$$\hat{\mathbf{S}} = \mathbf{WX} \cdots (2)$$

where matrix $\hat{\mathbf{S}}$ represents the independent components that are statistically independent from each other, and matrix **W** is the separating matrix. Matrix **W** is optimized so that $\hat{\mathbf{S}}$ is statistically independent of each other.

2.3 Proposed component selection method

We propose a new component selection method that can perform automatic, quantitative selection. In our previous study[1], we proposed a component selection method that takes the synchronization of correlation function peaks of independent components and an ECG signal. However, in this study, the proposed method does not require the ECG signal. Instead, the proposed method utilizes the autocorrelation function of the independent components after completing the ICA and the average of the peak values, as follows.

1. Calculate the autocorrelation function of the independent components separated by ICA. The equation of the autocorrelation function is:

$$R_{(t)} = \frac{1}{N}\sum_{i=0}^{N} \frac{\left(\hat{s}_i - \bar{\hat{s}}\right) \times \left(\hat{s}_{i+t} - \bar{\hat{s}}\right)}{\sqrt{\left(\hat{s}_i - \bar{\hat{s}}\right)^2} \times \sqrt{\left(\hat{s}_{i+t} - \bar{\hat{s}}\right)^2}} \cdots (3)$$
$$(0 \le t \le T - 1)$$

where $\hat{\mathbf{s}}_i$ are the rows of matrix $\hat{s}$, which contains independent component data, $\bar{\hat{s}}$ is the average of $\hat{s}_i$, N is the sampling number (500 points = 1 s), T is the measurement time, and t is the shifted time.

2. Detect peaks of the autocorrelation function. We maintain peaks that have the same timing as other independent components because independent components containing the MCG signals have the same timing. We eliminate peaks if the peak interval is below 0.5 s (2 Hz) because the peak interval of MCG signals is approximately 0.5–2 Hz.
3. Calculate the averages of the chosen peaks (AP) of the independent components.

After performing these processes, we set the threshold AP values and distinguish between the independent components representing MCG signals and those corresponding to noise using the threshold.

3. Simulation method

The simulation method had two objectives. First, to assess the difference in the AP values between the MCG signals and the noise components. The second was to compare the component selection performed by the proposed method with the highest accuracy of noise reduction (HANR) method and the method of subjective judgment from waveforms. We explain the method used to determine the HANR method in section 3.2.

3.1 Simulation data

The MCG data was measured using a 64-channel (8×8) SQUID magnetometer in a magnetically shielded room (MSR). To reduce the noise, the MCG data were averaged 150 times. The averaged data represent the ideal data. Fig. 1 shows the ideal data of the 51 channel (highest amplitude position). The noise data were also measured using the same SQUID magnetometer with applying environmental magnetic noise via a coil in the MSR. Fig. 2 shows the applied noise data that was measured outside the MSR using a fluxgate. The simulation data were mixed with the ideal data and the noise data with signal-to-noise ratios (SNRs) of 0 dB, -10 dB, and -20 dB. The sampling frequency of the simulation data was 500 Hz, and the simulation data were 10 s (5000 data points). The equation of the SNR is

$$\mathrm{SNR} = 20\log_{10}\frac{A_s}{A_n}\ [\mathrm{dB}]$$

where A_s is the peak amplitude of the QRS-complex, which is the highest amplitude sensor position for the ideal data, A_n is the zero-to-peak amplitude of the noise data. The utilized data are shown in the following figures (Figs. 1 and 2).

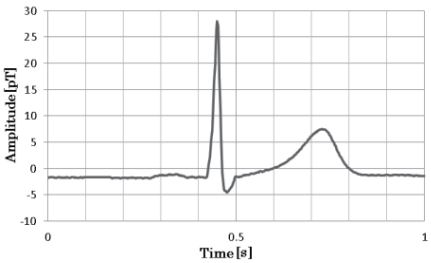

Fig. 1 Ideal data of highest amplitude position

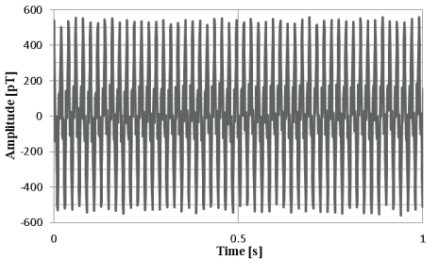

Fig. 2 Noise data that was measured outside the MSR

3.2 Simulation process

The simulation was performed using the same process as the noise reduction method using the ICA, which is explained in section 2. The specific simulation process is as follows:

1. Apply the PCA to the simulation data (64 channels × 5000 points) for whitening.
2. Perform dimensional contraction on the whitening data. We selected eight components from higher contribution ratios. The eight components had 99.9% or more information amount at all simulation data.
3. Apply the ICA to the whitening data (eight components selected in step 2) to separate the independent components.
4. Distinguish the independent components, which represent the noise, from the independent components, which represent the MCG signals, using the proposed automated method; thereafter, select the independent components that represent MCG signals.
5. Apply an inverse process to reconstruct the measurement data using the selected independent components.

To evaluate the proposed method, we calculated the correlation coefficient between the ideal data and the reconstructed data. The reconstructed data are the results of the noise reduction using the proposed method, the selection pattern with the HANR method, and the experimental judgment from waveforms. The HANR method was determined from among all selection patterns in all the simulations. The selection pattern of the HANR method was the one that had the highest correlation coefficient between the ideal data and the reconstructed data.

4. Simulation results

4.1 Peak timing

Fig. 3 shows an example of the independent components (left side) and the autocorrelation functions (right side). The figures in Fig. 3 show three characteristic components from eight independent components. The figure at the top is characteristic of the QRS-complex; the figure at the center is characteristic of a T-wave; the figure at the bottom is one of the noise components. There are differences between the stationary signals and the random signals at peak values and peak timings. In case of the stationary signals, peaks are clearly defined because the autocorrelation function gives high values only when they correspond to peak timings. However, in case of the random signals, peaks are not clearly defined because the autocorrelation function exhibits high values randomly.

Fig. 4 shows the peaks of the autocorrelation function. These figures are same as the ones on the right side of Fig. 3. The upper two signals have the same peak timings, while the lower signal exhibits random peak timings. Hence, we can determine the peak timings that represent the MCG signals.

4.2 AP values

Figs. 5-7 show the AP values of the independent components of the simulation data with SNRs of 0 dB, -10 dB, and -20 dB, respectively. The gray bars indicate the noise components, and the black bars indicate the MCG signal components that were chosen by the selection pattern of the HANR method. In Figs. 5-7, the AP values of the MCG signal components are higher than those of the noise components. The lower AP values of the MCG signal components, the lower SNRs.

Fig. 8 shows the AP values of all the independent components (8 × 3 = 24 components) of the simulation data at all SNRs tested. The 24 independent components have been arranged in descending order of the AP value. All AP values of the MCG signal components were higher than those of the noise components when the noise and MCG signal components were distinguished by the selection pattern of the HANR method. The boundary between the MCG signal and the noise components is at the AP value of 0.6; the MCG signal components had the AP values > 0.6 while noise components had the AP values < 0.6.

4.3 Comparison with waveforms

Figs. 9-11 show the waveforms of the independent components of the simulation data at SNRs of 0 dB, -10 dB, and -20 dB, respectively.

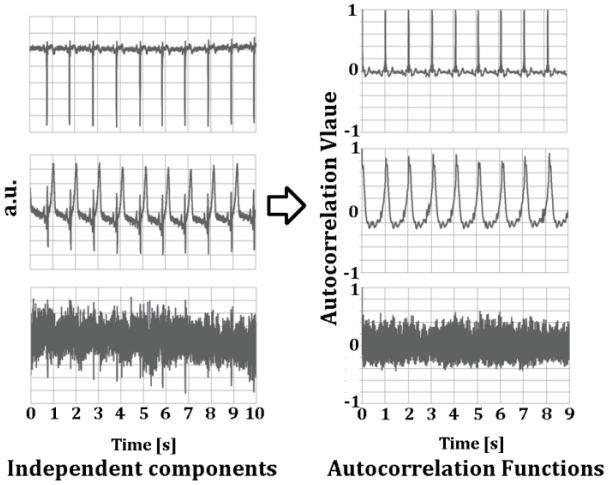

Fig. 3 Example of autocorrelation transformation

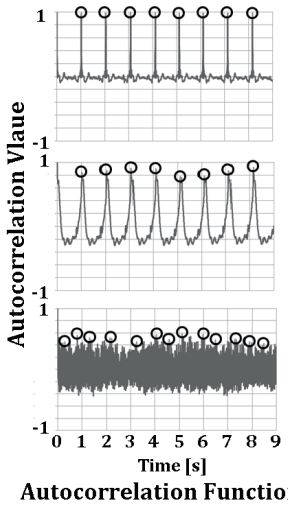

Fig. 4 Peaks of autocorrelation functions

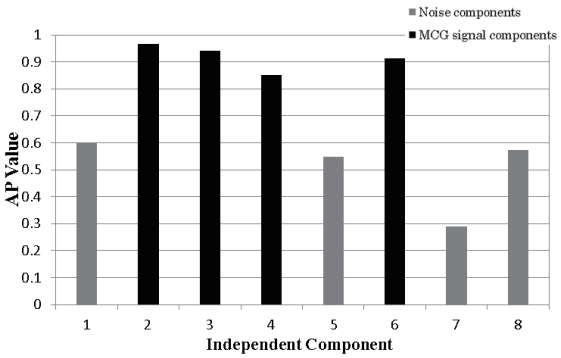

Fig. 5 AP value of simulation data at 0 dB

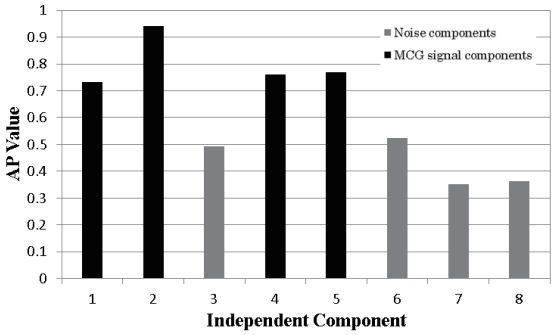

Fig. 6 AP value of simulation data at -10 dB

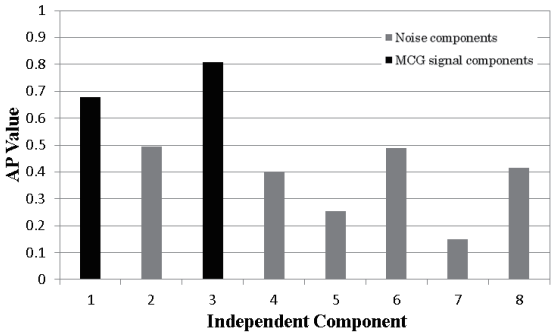

Fig. 7 AP value of simulation data at -20 dB

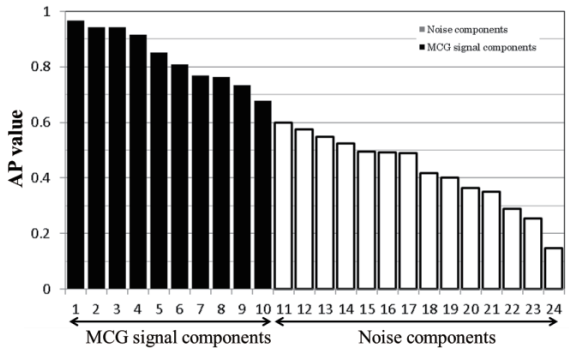

Fig. 8 AP value of all simulation data

In Fig. 9 (0 dB), performing a subjective judgment from the waveforms would lead to the selection of Nos. 2, 3, 4, and 6 as the MCG signals. This selection pattern is identical to the selection pattern of the HANR method. It is also identical to the result using high or low AP values, shown in Fig. 5.

Similarly, the subjective judgment method would select Nos. 1, 2, 4, and 5 in Fig. 10 (-10 dB) and Nos. 1 and 3 in Fig. 11 (-20 dB) as the MCG signals. Moreover, these selection patterns are the same as those determined by the HANR method and the results using high or low AP values, as shown in Figs. 6 and 7.

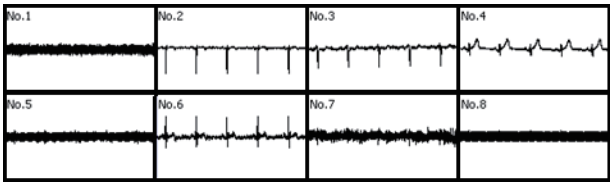

Fig. 9 Waveform of independent components (0 dB)

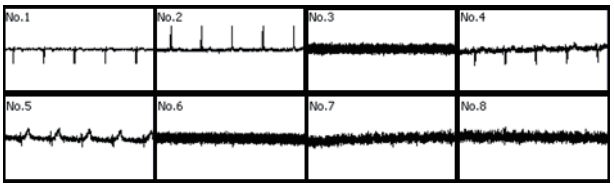

Fig. 10 Waveform of independent components (-10 dB)

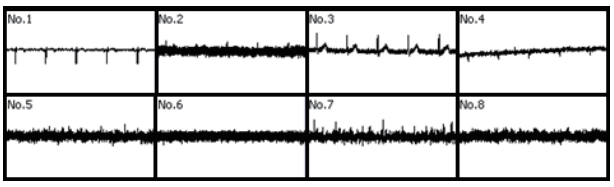

Fig. 11 Waveform of independent components (-20 dB)

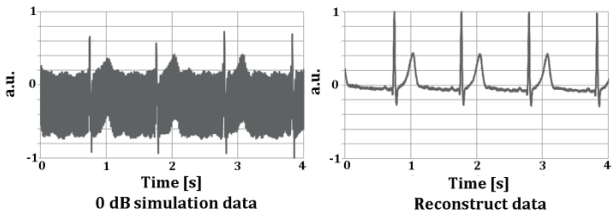

Fig. 12 Result of the noise reduction (0 dB)

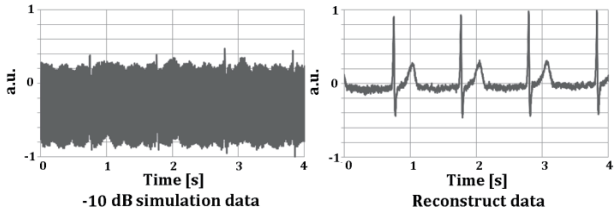

Fig. 13 Result of the noise reduction (-10 dB)

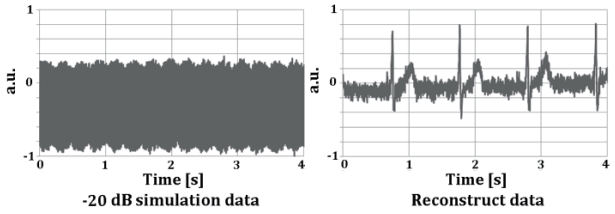

Fig. 14 Result of the noise reduction (-20 dB)

4.4 Waveform of noise reduction

Figs. 12-14 show examples of the waveforms before and after noise reduction for the simulated data at SNRs of 0 dB, -10 dB, and -20 dB, respectively. The SNRs of the reconstructed data were 33.98 dB, 19.17 dB, and 13.56 dB for the simulated data at SNRs of 0 dB, -10 dB, and -20 dB, respectively. The SNRs were calculated from the R-wave peak values (signal) and the baseline amplitudes (noise).

5. Discussion

First, we discuss some relevant conditions for successfully applying the HANR method. In many cases, this method can distinguish the MCG signals from the noise components. This method rejects components that have periods (interval of autocorrelation peaks) of 0.5 s (2 Hz) or less, because the MCG signals have a period of 0.5 s or more. However, this method cannot distinguish, when noise with a period of 0.5 s or more is applied.

Second, we discuss the threshold of the HANR method. The threshold is dependent on the SNR. Hence, as it is possible to approximate the SNR from the amplitude of the environmental magnetic noise and the general MCGs, we will determine the threshold value on which it is based. If the SNR is in the range 0~-20 dB, we can perform this method utilizing the threshold (0.6). Based on the threshold (0.6), Fig. 15 shows the SNRs of the reconstructed data for which the threshold ranged from 0.4 to 0.9. The method was able to maintain the accuracy of noise reduction when the threshold ranged from 0.6 to 0.66.

Third, we discuss the processing time. In this time, these processes were performed by two programs to check the AP values or other selection patterns. The total processing time was approximately 30 s when the method was performed utilizing the two programs. The total time was not considerably long as compared to the measurement time (a few minutes).

Finally, we discuss the application of this method for heart disease. In case of arrhythmia, MCGs can be measured utilizing the proposed method because independent components that are representing MCG signals have same peak timings. However, MCGs cannot be acquired using the proposed method, if we cannot get those synchronization.

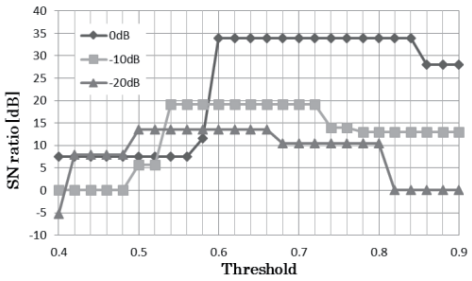

Fig. 15 SNRs with respect to varying threshold

6. Summary

We proposed a new method of component selection using ICA to perform the selection automatically and quantitatively. The ability of this proposed method to distinguish independent components is on par with that of the HANR method and the subjective judgment of waveforms of independent components.

The boundary between the noise and the MCG signal components was at the AP value of 0.6, which was determined using the HANR method. The noise components had AP values of 0.6 or less, while the MCG signal components had AP values of 0.6 or greater.

Acknowledgements

This work was partly supported by the Japan Society for the Promotion of Science through a Grant-in-Aid for Scientific Research (C) 26350535 and 25462573, and by the Natural Sciences and Engineering Research Council of Canada (NSERC).

References

1) K. Kobayashi, K. Oyamada, M. Yoshizawa, and Y. Uchikawa: J. Magn. Soc. Jpn. (2010), **34**, 156-160
2) K. Oyamada, K. Kobayashi, M. Yoshizawa, and Y. Uchikawa: J. Magn. Soc. Jpn. (2010), **34**, 146-150
3) D. P. Acharya and G. Panda: IETE Tech. Rev. (2008), **25**, 320-332
4) S. Comani, D. Mantini, P. Pennesi, A. Lagatta, and G. Cancellieri: Comput. Methods Programs Biomed. (2004), **75**, 163-177
5) Y. Sevim and A. Atasoy: Turk. J. Elec. Eng. & Comp. Sci. (2011), **19**, 657-666
6) B. Mijovic, M. Vos, I. Gligorijevic, J. Taelman, and S. Huffel: IEEE Trans. Biomed. Eng. (2010), **57**, 2188-2196
7) P. Comon: Signal Processing by Elsevier B.V. (1994), **36**, 287-314
8) A. Hyvärinen, J. Karhunen, and E. Oja: Independent Component Analysis (2001) by John Wiley & Sons, Inc.

Received Oct. 25, 2015; Accepted Dec. 26, 2016

Journal of the Magnetics Society of Japan

Vol. 41 No. 2 (通巻第 290 号) 2017 年 3 月 1 日発行

Vol. 41 No. 2 Published Mar 3, 2017

by the Magnetics Society of Japan
Tokyo YWCA building Rm207, 1–8–11 Kanda surugadai, Chiyoda-ku, Tokyo 101–0062
Tel. +81–3–5281–0106 Fax. +81–3–5281–0107

Printed by JP Corporation Co., Ltd.
2–3–36, Minamikase, Saiwai-ku, Kanagawa 212–0055
Advertising agency: Kagaku Gijutsu-sha

発行：（公社）日本磁気学会 101–0062 東京都千代田区神田駿河台 1–8–11 東京YWCA会館 207 号室
製本：（株）ジェイピーコーポレーション 212–0055 神奈川県川崎市幸区南加瀬 2–3–36 Tel.（044）571–5815
広告取扱い：科学技術社 111–0052 東京都台東区柳橋 2–10–8 武田ビル 4F Tel.（03）5809–1132